On the mechanism of visible-light accelerated methane dry reforming reaction over Ni/CeO_{2-x} catalysts

Kristijan Lorber[1,3], Janez Zavašnik[2], Jordi Sancho-Parramon[4], Matej Bubaš [4], Matjaž Mazaj[1] and Petar Djinović[1,3]*

[1]Department of Inorganic Chemistry and Technology, National Institute of Chemistry, Hajdrihova 19, SI-1000 Ljubljana, Slovenia

[2]Jožef Stefan Institute, Jamova cesta 39, SI-1000 Ljubljana, Slovenia

[3]University of Nova Gorica, Vipavska 13, SI-5000 Nova Gorica, Slovenia

[4]Ruđer Bošković Institute, Division of Materials Physics, Bijenička cesta 54, 10000 Zagreb, Croatia

*Corresponding author email: petar.djinovic@ki.si

Abstract

The methane dry reforming reaction (DRM) converts methane and CO_2 into syngas, a mixture of H_2 and CO. When illuminated by white light, the $2Ni/CeO_{2-x}$ catalyst enables conversions of both CH_4 and CO_2 beyond thermodynamic equilibrium, while the energy efficiency reaches 33 %. The DRM reaction is sustained in a purely photocatalytic mode without external heating when illuminated by 790 mw/cm^2 of white light with CH_4 and CO_2 rates equaling 0.21 and 0.75 $mmol/g_{cat}$*min, respectively. At a constant catalyst temperature of 400 °C, the reaction selectivity expressed as H_2/CO ratio increases from 0.23 to 0.59 in light-assisted mode compared to the experiment in the dark. The theoretical analysis of Ni/CeO_{2-x} optical properties agree with *in-situ* UV-Vis DRS results and show that the presence of partly reduced Ce^{3+} sites is crucial for extending the optical absorption of Ni/CeO_{2-x} into the visible light range. The strong electromagnetic near field enhancement was identified as the dominant source of visible-light-induced rate acceleration and occurs mainly over nickel nanoparticles which are the active sites for methane activation. This work identifies Ni/CeO_{2-x} photocatalyst as highly efficient for boosting methane activation by visible light illumination under mild conditions.

Keywords: photocatalytic methane activation, Ni/CeO_{2-x}, selectivity, visible light, reaction mechanism.

Introduction

Methane dry reforming reaction (DRM, $CH_4 + CO_2 \leftrightarrow 2CO + 2H_2$) represents an attractive pathway for converting methane (an abundant and cheap hydrocarbon) and CO_2 (greenhouse gas) into a mixture of H_2 and CO (syngas). DRM is among few catalytic CO_2 reduction processes (such as CO_2 hydrogenation to methanol, reverse water gas shift and Sabatier reaction), which could be implemented on a global megaton scale to mitigate anthropogenic CO_2 emissions and thus minimise its impact on climate change.[1,2] Syngas is widely used in the petrochemical industry for synfuel production via the Fischer-Tropsch process, as well as for hydrogenation, hydroformylation and carbonylation reactions.[3] The downsides of the DRM reaction are high endothermicity (ΔH_r= -247 kJ/mol, ΔG_{298K}=171 kJ/mol) and unfavourable thermodynamic equilibrium values at low reaction temperatures, which limit achievable conversion and hydrogen selectivity. The DRM reaction has been extensively studied at high temperatures (>600 °C) over transition (Ni, Co and Fe), as well as noble metal catalysts (Ru, Rh, Pt and Pd).[4] Nickel exhibits high activity for methane activation[5] and when dispersed in the form of nanoparticles over CeO_2, yields an affordable and outstandingly active DRM catalyst.[6,7] Also, if the nickel cluster size is maintained below 5 nm, carbon accumulation during the reaction can be avoided,[8] which overcomes a substantial hurdle in the industrial application of this reaction.[9] Abundance of oxygen vacancies on ceria, manifested through its redox activity,[10] is regarded as crucial for kinetic balancing of carbon accumulation and gasification reactions during DRM, preventing carbon accumulation on catalysts and consequent deactivation.[11,12] In the past years, catalysis over nano-shaped ceria revealed notable improvements of activity in several reduction and oxidation reactions,[13] which appear to be correlated with ease of oxygen vacancy formation over its different terminating facets.[13,14] Activity dependence on ceria shape was also observed in DRM reaction over Ni/CeO_2 catalysts.[15]

Photocatalysis is a promising pathway for converting intermittent light (photon energy) into storable chemical energy.[16–18] Illumination of the catalyst can significantly accelerate the reaction rates, and conversions beyond the thermodynamic equilibrium can be achieved due to non-thermal, vibrational and electronic stimulation of adsorbed reactants and reaction intermediates.[19,20] Thus, (photo)catalytic reactions can be performed at lower temperatures and pressures, which is often beneficial in terms of product selectivity, catalyst stability as well as process cost and design.

Several papers investigating plasmonic and non-plasmonic metals (Au, Pd, Pt and Rh) supported on black titania, Al_2O_3, TaON, Ta_3N_5 and SiO_2 report of increased H_2 and CO yields during photocatalytic, compared to thermocatalytic DRM reaction.[21–24] Shoji et al.[19] report that $Rh/SrTiO_3$ catalyst enables methane and CO_2 conversions far beyond thermodynamic equilibrium under UV light irradiation and without additional heating. The photocatalytically produced syngas contained an equimolar H_2 and CO content, which is not achievable during thermocatalytic DRM reaction due to a large fraction of

hydrogen converted to water by the kinetically dominant RWGS reaction.[25]

Halas et al.[26] utilised plasmonic Cu antennas decorated with Ru single sites, which enabled up to a 5-fold increase of methane reaction rate compared to thermocatalysis, and 100 % H_2 selectivity when the catalyst was illuminated by >16 W/cm^{-2} of white light.

It is becoming clear that visible and UV light have a notable benefit on catalytic activity and selectivity in DRM reaction over noble metals (Rh,[19] Au,[21,23] Pt,[22] Pd,[23] Ru,[26]). From an academic, industrial, and practical perspective, a strong photocatalytic response in DRM reaction over transition metal/semiconductor photocatalysts that can be produced with a scalable synthesis method is highly desired.

This work investigates the applicability of Ni/CeO_2 nanorod catalyst for visible-light-driven DRM reaction at mild conditions and analyses the underlying mechanisms. The *in-situ* UV-Vis DRS analysis showed facile catalyst activation by visible light, confirmed by simulation of its electromagnetic properties. The consequences of catalyst illumination by 790 mW/cm^2 of white light ($400 < \lambda < 700$ nm) were up to an 8.5-fold increase in methane rate and improved H_2 selectivity (H_2/CO increased from 0.23 to 0.59) compared to thermocatalytic DRM at a constant catalyst temperature of 400 °C. Also, methane and CO_2 conversions beyond the thermodynamic equilibrium were achievable at temperatures below 250 and 300 °C, respectively.

Experimental

The selection of ceria nanorod morphology as the catalyst support is based on our preliminary screening of nickel on ceria nanorod and nanocube catalysts (Fig. S 1). The nanorod based catalyst was more active, accumulated far less carbon and maintained a higher fraction of Ce^{3+}, which is important for visible light absorption.[27] CeO_2 nanorods were synthesised according to Zabilskiy et al.[28] by dissolving 53.8 g of NaOH (99 % purity, Merck) in 140 mL of ultrapure water. Then, 84 mL of the aqueous solution containing 4.9 g of $Ce(NO_3)_3 \cdot 6H_2O$ (99 % purity, Sigma-Aldrich) was added under vigorous stirring. The suspension was stirred for an additional 30 min and transferred into Teflon® lined stainless steel autoclaves (volume ~35 mL each), where it was aged for 24 h at 100 °C in a laboratory drier. After autoclave quenching, the suspension was filtered, dried overnight at 70 °C and calcined in air (4h at 450 °C, heating ramp of 5 °C/min, Nabertherm P330).

Different nickel loadings (0.5, 1, 2 and 4 wt. % nominal) were deposited by adding 2 % NH_4OH solution to the aqueous suspension containing CeO_2 nanorods and an appropriate amount of dissolved $Ni(NO_3)_2$, Sigma Aldrich, purity 99%. The pH of the suspension was raised to 9.5 over the course of 2 h, and stirring was maintained at 400 rpm for an additional 2 h after the final pH was reached. The efficiency of nickel deposition was verified spectrophotometrically by analysing the mother liquor using a Spectroquant® NOVA60 analyser (Merck). In all cases, the efficiency of nickel

deposition was above 98 %, and nominal loadings were considered actual. Finally, the suspension was centrifuged, dried overnight at 70 °C in a laboratory drier, and calcined in air for 4 h at 450 °C (Nabertherm P330). The samples are denoted as CeO_2-R for the bare ceria support and xNi for nickel ceria nanorod catalysts, where "x" represents the nickel loading.

The *in-situ* UV-Vis DRS analysis was performed on the Lambda 650 apparatus (Perkin Elmer) equipped with a HVC-VUV-5 reaction chamber from Harrick. Finely powdered samples (~10 mg) were analysed in air at 25 °C and in 5% H_2/N_2 (flow of 10 ml/min, purity 5.0 by Messer) after dwelling the sample at 200 and 450 °C for 30 min. Spectralon® white standard was used to record the background.

The XRD analyses were performed on a Panalytical XP PRO MPD apparatus using $Cu_{\alpha 1}$ irradiation (λ=1.5406 Å) in the 2theta range between 10 and 80°, step size of 0.034° and and fully opened 100 channel X'Celerator detector.

Te H_2 adsorption experiments were performed on a IMI-HTP manometric sorption analyzer (Hiden Isochema Inc.). Prior the isothermal measurements, the catalyst samples were reduced *in-situ* in pure H_2 flow of 10 ml/min while ramping the reactor temperature at 5 °C/min to 350 °C. After the reduction pretreatmentlasting 16 h, the sorption isotherms were measured at 110 °C in the pressure range between 50 – 1000 mbar. The chemisorbed H_2 values were estimated from extrapolating the linear part of the H_2 desorption isotherm to zero pressure as described by Slowik et al.[29] and the average nickel particle size was adopted from Velu et al.[30]

The N_2 physisorption technique (Tristar II apparatus from Micromeritics) was used to analyse BET specific surface area, total pore volume and average pore size (BJH method) of the synthesised catalysts. Before analysis, the samples were degassed 1 h at 90 °C, followed by 4 h at 300 °C in N_2 flow (purity 6.0, Linde) on a SmartPrep accessory (Micromeritics).

Thermogravimetric analysis (TGA) was used to quantify carbon accumulated on the catalyst during the reaction. The samples were heated in airflow (25 ml/min) from 50 to 800 °C with a 10 °C/min ramp (Perkin Elmer, model STA6000). Carbon mass was calculated from the mass difference before and after analysis.

H_2-temperature programmed reduction (H_2-TPR) was performed on an AutoChem 2920 apparatus to analyse the reduction of materials and quantify the amount of consumed H_2. Before analysis, the samples were *in-situ* pretreated in synthetic air at 300 °C for 15 minutes. After cooling to 10 °C, the atmosphere was changed to 5% H_2/Ar (25 ml/min), and a temperature ramp of 10 °C/min was used to heat the sample (100 mg) to the final temperature of 550 °C. H_2 consumption was analysed with a TCD detector, and a LN_2/isopropanol cold trap was used to remove water vapour and eliminate its contribution to H_2 quantification.

For TEM analyses, powder samples were first dispersed in absolute ethanol and sonicated to prevent

agglomeration of the nanoparticles. Such prepared suspension was transferred onto commercial lacey-carbon Cu support grids. TEM analyses (conventional TEM micrographs, HR-TEM and electron diffraction patterns) were performed on a LaB_6 JEM-2100 microscope (Jeol Inc.), operated at 200 kV and additionally equipped with an energy-dispersive X-ray spectrometer (EDS, model EX-24063JGT, Jeol Inc.). TEM micrographs were recorded by Orius SCD-1000 (Gatan Inc.) slow-scan CCD camera.

Simulation of electromagnetic properties of bare CeO_2 rods, spherical Ni particles and Ni/CeO_2 nanorod catalysts was done using the MNBEM implementation of the boundary element method.[31] Optical constants for Ni, oxidised and reduced ceria were taken from literature[32,33]. In all calculations, the CeO_2 rods are assumed to be in an air-like environment. Calculations were done averaging over different light polarisation directions with respect to the rod axis to simulate a random orientation of nanorods.

Catalytic tests were performed in a modified reaction chamber (HVC-MRA-5, Harrick, Figs. S2 and S3) between 180 and 470 °C. During thermocatalytic experiments, the catalyst temperature was varied in 10-50 °C increments by changing the power output of the electric heater. During light-assisted experiments, the catalysts were illuminated by 790 mw/cm^2 of white light, and the catalyst temperature was varied by changing the power output of the electric heater. Schott KL2500 LED source ($400 < \lambda < 700$ nm, Fig. S4) was used for catalyst illumination, equipped with an optic fibre with a 9 mm active diameter and light focusing lenses (Thorlabs Inc.), which concentrated the light to a spot equal to the catalyst pellet diameter (4.5 mm) with a maximum intensity of 790 mW/cm^2 (measured by Thorlabs PM100D photometer). For all tests, 2 mg of finely powdered catalyst was used, which formed a round pellet measuring 4.5 mm in diameter and 0.5 mm in thickness. The catalyst was positioned on top of a 1 mm thick layer of powdered SiC (Sicat, 30-150 μm) to improve heat transfer from the furnace to the sample and minimise radial temperature gradient in the catalyst layer. The catalyst temperature was measured with a 0.25 mm thermocouple (Omega Engineering Inc., model SCASS-010U-12) located about 0.2 mm below the illuminated catalytic surface. Before reaction, the catalysts were activated *in-situ* in a 10 ml/min flow of 5% H_2/N_2 (Messer, purity 5.0) at 450 °C for 30 min. Afterwards, the atmosphere was switched to CH_4 and CO_2 (Linde, purity 5.0 and 5.3, respectively) with a flow of 10 ml/min each (WHSV= 600 L/g_{cat}*h). All catalytic tests were performed in the kinetic regime to ensure intrinsic activities are reported. Analysis of gas leaving the photocatalytic reactor was performed by GC (model 490, equipped with MS5A and PPU columns by Agilent). Each reported activity point is a calculated average of at least five analytical repetitions.

Results and discussion

The specific surface area of CeO_2-R with the value of 84 m^2/g changed negligibly after the nickel

deposition, regardless of its loading (0.5-4wt. % of Ni). The average pore size determined by BJH method defining interparticle porosity was found to be 11 nm for bare CeO_2-R and increased slightly for the Ni/CeO_2 catalysts (13-16 nm, Table S1).

The XRD analysis (Fig. S5) confirmed the presence of the Face Centered Cubic (*fcc*) fluorite-type ceria phase (PDF 00-034-0394) in bare CeO_2 support and Ni/CeO_2 catalysts. The average CeO_2 crystallite size of 11 nm was calculated by the Scherrer equation for bare CeO_2-R, and this value remained identical after deposition of nickel. No diffraction peaks belonging to NiO or metallic nickel were observed in any of the samples, suggesting its presence in the form of small nanoparticles.

TEM analysis of bare CeO_2-R support (Figs. 1A and 1B) and 2Ni catalyst (Fig. 1D and 1E) confirmed the presence of ceria in the shape of nanorods, which are about 8-15 nm thick and 100-200 nm long. The nanorod thickness corresponds well with the average crystallite size calculated from XRD. The CeO_2 nanorod morphology is dominated by (111) facets, with (100) and (110) facets exposed only at the tips of the nanorods, contributing less than 10% to the overall surface area. Phase identification of fluorite-type CeO_2 was confirmed by SAED (Fig. 1C). In the 2Ni catalyst sample, nickel was visualised as polyhedral nanoparticles decorating the surface of ceria nanorods (Figs. 1E and 1F). Nickel particle size, measured from the HR-TEM micrographs, range between 5.1 - 6.5 nm, matching the values obtained by the H_2 chemisorption-TPD technique (Table S 2).

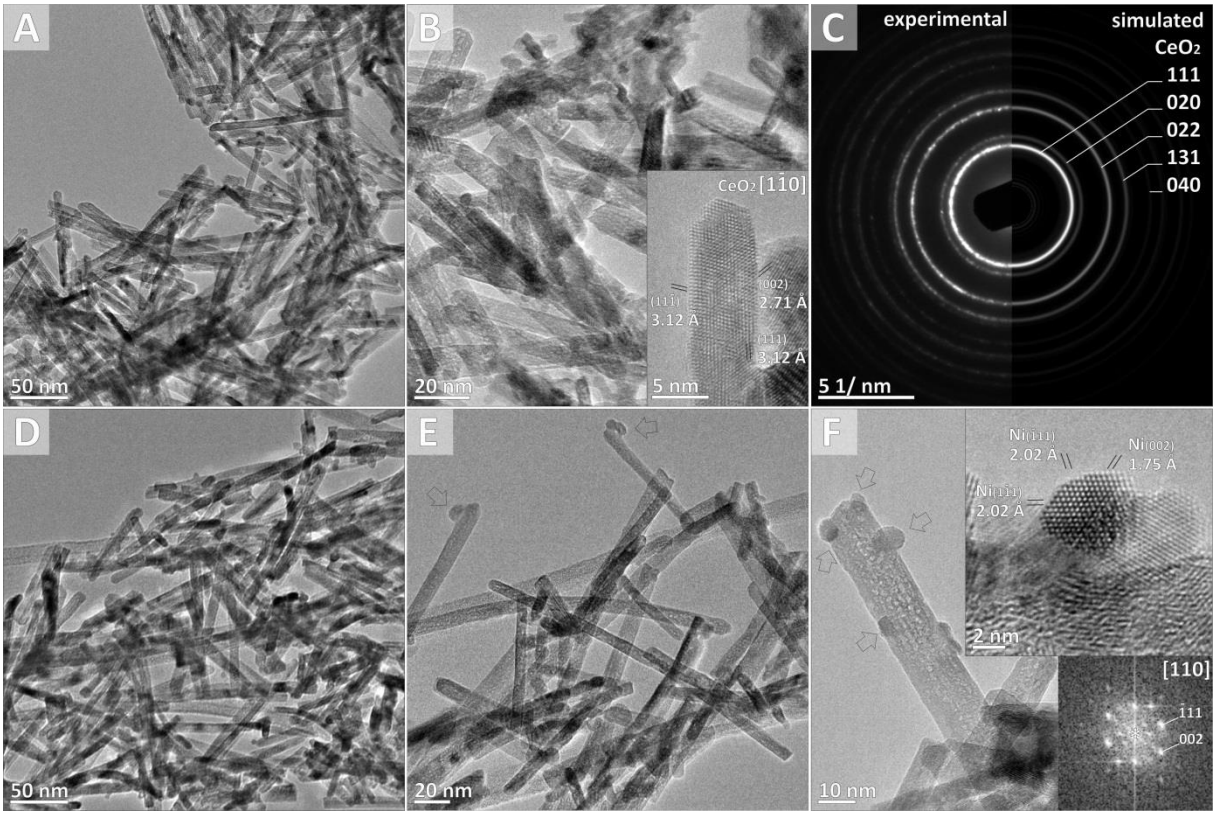

Figure 1. TEM micrographs of bare CeO_2-R support (A, B) and 2Ni catalyst (D, E and F). The ceria

nanorods are crystalline, showing well-developed crystal faces (B, inset). Experimental SAED pattern, recorded over multiple particles, corresponds to pure CeO_2 phase with *Fm-3m* (No. 225) space group (C). After Ni deposition, the shape and morphology of nanorods are preserved (D, E), with surface-attached nanoparticles marked by arrows (E); the fast Fourier transform (FFT), calculated from phase-contrast HR-TEM micrograph (F, inset) corresponds to cubic Ni phase with *Fm-3m* (No. 225) space group.

The redox properties of CeO_2 are indicative of a reversible generation of oxygen vacancies and Ce^{3+} sites, which serve as active sites for dissociative CO_2 adsorption[7,13]. The reducibility of CeO_2 depends on the shape of its crystals, their size and thermal history and governs on time coke gasification during DRM, which prevents catalyst deactivation.[13,34,35] For the photocatalytic application of ceria, the existence of Ce^{3+} ensures the occupation of energy levels in the 4f orbital. The 4f orbital lies about 3 eV above the valence band maximum, making electron promotion from the 4f orbital to the conduction band achievable by visible light photons.[27]

During H_2-TPR analysis of Ni/CeO_2 catalysts (Fig. S6), the reduction started already at 30 °C, whereas for bare CeO_2 nanorods, it was initiated much later at 250 °C. The H_2 consumed during reduction increased progressively with nickel content in the catalysts (Table S2). Based on the quantification of H_2 consumed until 550 °C, 17 % of Ce^{4+} was reduced to Ce^{3+} in bare CeO_2-R, and this value was very similar also for 1Ni and 2Ni catalysts (19 and 17 %, respectively, Table S2), and decreased to 9 % in 4Ni sample. To summarise, the Ni/CeO_2 catalysts contain a notable fraction of reduced Ce^{3+} sites in reducing atmosphere and in the temperature range relevant for catalytic reactions performed in this work.

The *in-situ* UV-Vis DRS was used to analyse the ability of the Ni/CeO_{2-x} catalysts to absorb visible light under, which is a prerequisite for photocatalytic activity. The optical bandgap of pristine CeO_2 and Ni/CeO_2 catalysts at 25 °C in air decreased slightly, from 3.21 to 3.12 eV with increasing Ni content from 0 to 4 wt. % (Fig. 2 and Figs. S7 and S8). Upon heating the samples in a 5 % H_2/N_2 atmosphere to 450 °C, the bandgap values of Ni/CeO_{2-x} samples decreased to values between 2.92 and 2.79 eV (Fig. 2), making them suitable for visible light harvesting. The thermal contribution to bandgap narrowing is proportional to Boltzmann constant multiplied by the temperature change (8.617×10^{-5} eV/K*ΔT) and is equal for all samples: 0.015 and 0.037 eV when heated from 25 to 200 and 450 °C, respectively. The observed bandgap narrowing is larger (0.21 eV for bare CeO_2 and 0.33 eV for 4Ni when heated in reducing atmosphere from 25 to 450 °C, Fig. 2), revealing the change is dominated by chemical alteration (reduction) of the catalysts. The partial reduction caused a gradual change of colour from pale brown to dark grey, resulting in a strong absorption throughout the visible range spectrum (Fig. S7). This sub-bandgap absorption was observed as a broad peak centered between

500 and 600 nm for all Ni/CeO_{2-x} catalysts in reducing atmosphere. Increasing the nickel content and temperature in the reductive atmosphere is favourable for both optical bandgap narrowing and increased sub-bandgap absorption of Ni/CeO_{2-x} catalysts.

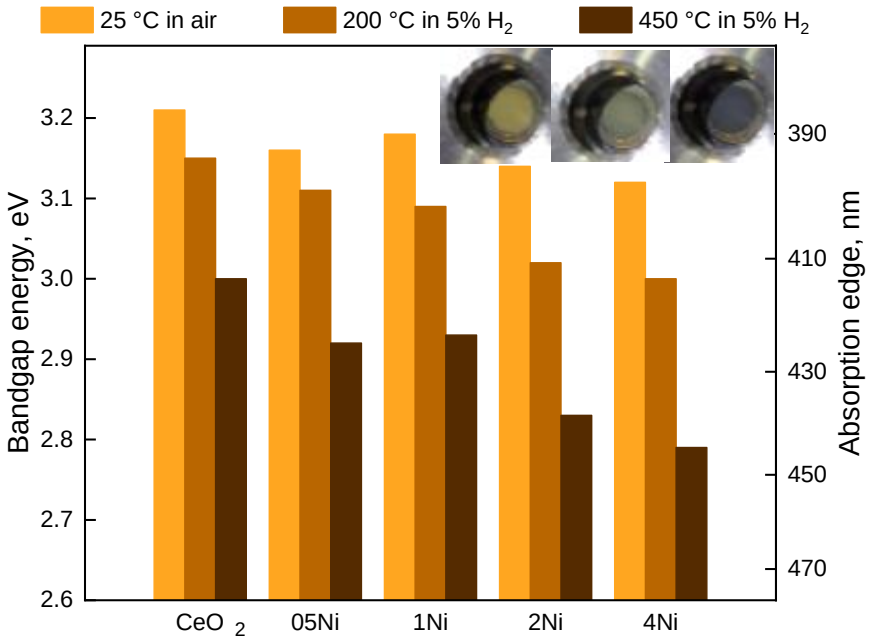

Figure 2. Bandgap energies for bare CeO_2-R and Ni/CeO_2 catalysts containing 0.5-4 wt. % Ni in air at 25 °C and 200 °C and 450 °C in 5 % H_2/N_2 atmosphere. Inset shows the 2Ni catalyst at mentioned temperatures and atmospheres.

Simulation of electromagnetic properties of bare CeO_2 nanorods (10x100 nm in size), bare spherical nickel nanoparticles measuring 6 nm and Ni/CeO_{2-x} nanorods is discussed in the following section to gain more insight into the occurring light-matter interactions.

The extinction cross-section as a function of wavelength for oxidised CeO_2 nanorods (Fig. S9) correlates well with the absorbance measurements of bare CeO_2 at 25 °C in air (yellow trace in Fig. S7). Over fully oxidised CeO_2, negligible absorption for wavelengths longer than 400 nm is expected. However, reduced CeO_{2-x} shows remarkable extinction in the visible part of the spectra due to the non-negligible extinction coefficient for energies below the band-gap[33], as was observed experimentally using *in-situ* UV-Vis analysis. We also computed the extinction cross-section of an oxidised CeO_2 rod covered by a thin (1 or 2 nm) external shell of partly reduced ceria (CeO_{2-x}).[36] Radial concentration gradients of cerium oxidation state (surface enrichment with Ce^{3+}) were previously experimentally observed in CuO/CeO_2 nanorod catalysts.[37] Our simulations showed a strong positive correlation between the thickness of the surface layer containing Ce^{3+} cerium sites and absorbance below the band-gap energy for CeO_{2-x}, expressed as a broad tail. It should be noted that a direct

comparison between the optical response of fully reduced (Ce_2O_3) and fully oxidised (CeO_2) ceria is difficult due to the lack of studies correlating oxidation state (exact fraction of Ce^{3+} and Ce^{4+}) and optical properties. In any case, our calculations and *in-situ* experimental data strongly indicate that partial reduction of CeO_2 and presence of Ce^{3+} leads to enhanced sub-band gap absorption.

The extinction cross-section of a bare 6 nm metallic nickel nanosphere is moderate when illuminated by wavelengths between 250 and 800 nm. (Fig. S10A.) The plasmon resonance in Ni nanoparticles strongly overlaps with the contribution of bound d electrons and can be hardly discerned in the extinction cross-section.[38] However, the plasmon-related enhancement of electromagnetic field intensity around the nanoparticle surface shows better-resolved features. The near-field response (like near field enhancement, Fig. S10B) of plasmonic nanoparticles is red-shifted with respect to the far-field response (like the extinction cross-section) for systems with significant losses[39]. However, in the case of nickel, the average and maximum near field enhancement is very moderate, making it a poor plasmonic metal.

Simulation of electromagnetic properties of partly reduced CeO_{2-x} rods decorated with one or five spherical 6 nm Ni nanoparticles (Figure 3A) shows that the presence of Ni nanoparticles does not significantly modify the absorption properties of the partly reduced ceria.

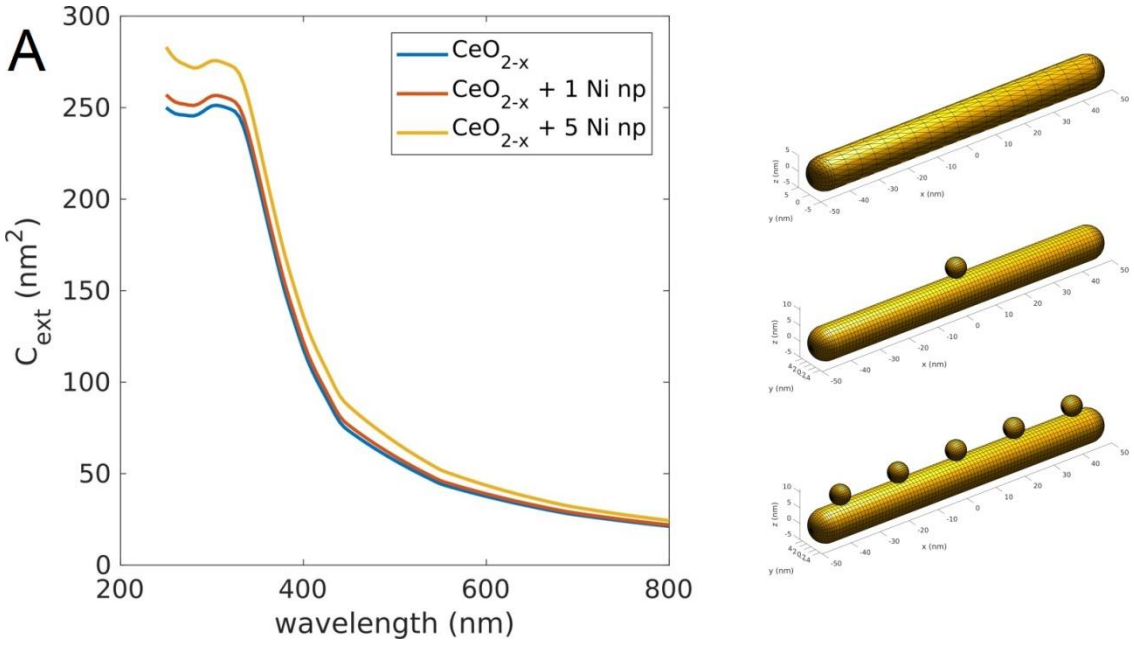

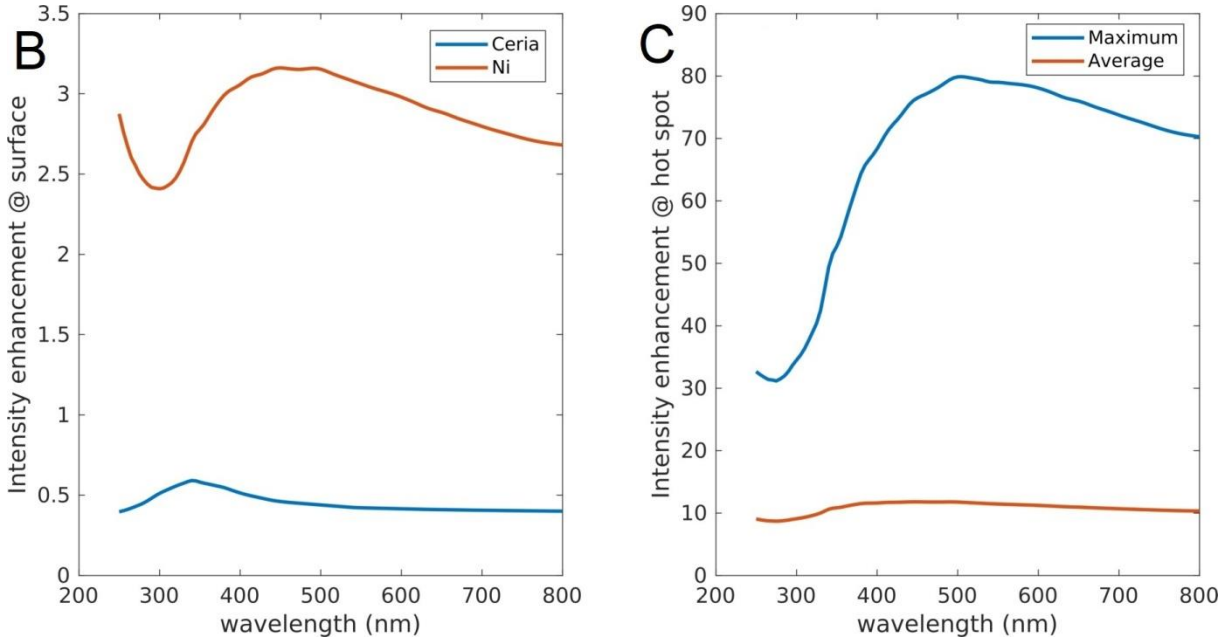

Figure 3. (A) Extinction cross section of bare CeO_{2-x} rods and decorated with 1 or 5 spherical nickel nanoparticles measuring 6 nm in diameter. Geometric scheme of the simulated structures is shown top right. Near-field intensity enhancements of a CeO_{2-x} nanorod decorated with one spherical nickel nanoparticle: (B) average enhancement calculated over Ni and CeO_{2-x} surfaces and (C) average and maximum enhancement calculated in the hot spot region (cubic volume of 64 nm^3 centered at the contact point between Ni and CeO_{2-x} nanorod).

The absorbance of CeO_{2-x} rods is 1 to 2 orders of magnitude larger than that of bare nickel nanoparticles (Figures S9 and S10A). Our simulations suggest that the experimentally observed remarkable increase of absorption below the bandgap of CeO_2 does not seem to be related to the presence of Ni nanoparticles. The average field enhancement over the Ni surface in the Ni/CeO_{2-x} system is comparable to the values obtained for individual Ni particles (Figs. 3B and S10B). However, the maximum field enhancement in the region around the contact point between Ni and CeO_{2-x} rod (Fig. 3C) is almost two orders of magnitude larger than the average value over the particle surfaces. Spatial analysis of near field enhancement shows that it amplifies strongly and very locally at the interface between CeO_{2-x} rod and Ni particles (Fig. 4), thus creating 'hot spots'[40]. This can have important consequences also for accelerating photocatalytic methane activation. Rodriguez et al. [41] report that at the interface between nickel and ceria, methane dissociation is strongly promoted through electronic perturbation of nickel, induced by the reduced ceria.

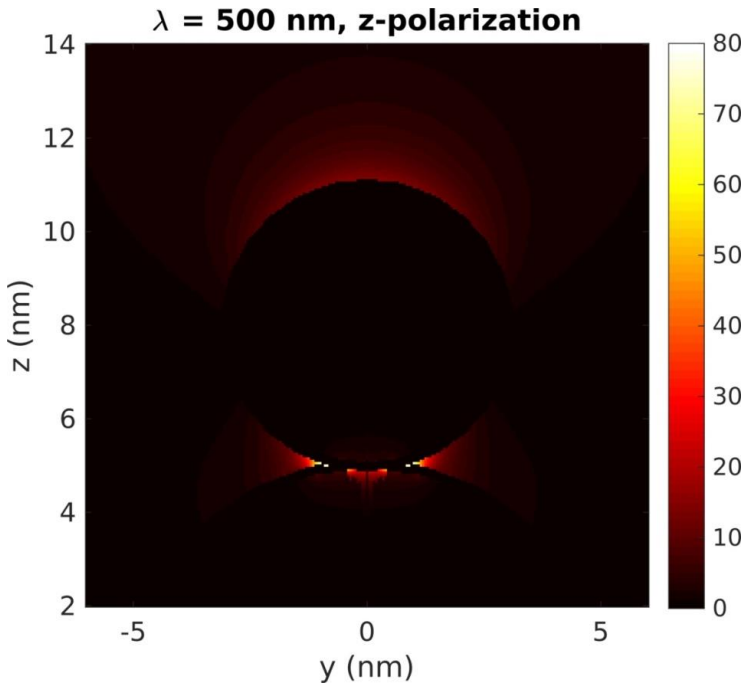

Figure 4. Spatial distribution of near field intensity enhancement for a Ni/CeO_{2-x} catalyst calculated at the wavelength where largest field enhancement takes place for light polarization parallel to the axis joining the Ni sphere and CeO_{2-x} rod.

Thermally driven DRM performance of Ni/CeO_{2-x} catalysts is shown in Figs. 5A and S11. The CH_4 and CO_2 conversion, as well as the H_2/CO ratio, increased with temperature and nickel content in the catalysts (05Ni < 1Ni < 2Ni ≈ 4Ni). Increasing the nickel content accelerates the DRM reaction rate due to the higher number of active sites for methane activation, which is the rate-determining step in the DRM reaction. The H_2/CO ratio and consequently H_2 selectivity increased in parallel with Ni particle size, likely due to the more dominant direct methane dehydrogenation pathway over larger nickel metallic particles. Over smaller Ni clusters, the contribution of the oxygen-assisted methane activation pathway at the nickel-ceria interface, which produces water, is more dominant.[42,43] This is due to oxygen spillover from the ceria to nickel and a relatively larger fraction of interface perimeter over smaller nickel particles. The amount of accumulated carbon on the catalysts during 6 h of the reaction was very low (0.1-0.2 wt. %) for 05Ni, 1Ni and 2Ni samples but increased sharply to 12 wt. % on 4Ni catalyst (Table S2). The carbon accumulation rate during DRM reaction is strongly dependent on nickel particle size and accelerates quickly as nickel size exceeds 5 nm.[8,12]

During the light assisted DRM experiments, the catalysts were constantly illuminated with white light (790 mW/cm^2), and the power output of the electric heater was adjusted to vary the catalyst temperature (Figs. 5B and S12). In the light assisted mode, the 2Ni catalyst was most active, followed by 4Ni. The CH_4 and CO_2 conversions were greatly accelerated compared to the thermocatalytic tests

315 at identical catalyst temperatures. Namely, the light assisted CH_4 rates over 2Ni catalyst were 4.26
316 and 1.58 mmol CH_4/g_{cat}*min at 460 and 362 °C, respectively. During thermally driven catalysis, these
317 values were 2.48 and 0.097 mmol CH_4/g_{cat}*min, respectively (Figs. 5C, S11A and S12A). Regardless of
318 nickel content, no CH_4 or CO_2 conversion could be identified below 347 °C during thermally driven
319 DRM. However, CH_4 and CO_2 rates of 0.2 and 0.8 mmol/g_{cat}*min were observed over 2Ni catalyst in
320 purely photocatalytic mode with no external heating (Fig. 5C). The purely photocatalytic rates over
321 2Ni catalyst are comparable to those achieved by Shoji et al.[19] over $Rh/SrTiO_3$ catalyst, irradiated by a
322 150 W Hg-Xe lamp at 200 °C.
323 Also, in the light assisted mode at temperatures up to 250 and 300 °C, respectively (Fig. 5B), the 2Ni
324 and 4Ni catalysts enabled CH_4 and CO_2 conversions well beyond the values predicted by
325 thermodynamic equilibrium. This is a consequence of catalyst excitation by photons, which provide
326 energy input in the form of vibrational and electron energy for activation of adsorbed reactant
327 species. The photocatalytic activity is limited by the number of photons provided by the light source,
328 whereas the thermocatalytic activity increases exponentially with increasing temperature according
329 to the Arrhenius law.[19,20,26] As a result, the highest photocatalytic gain was observed at low
330 temperatures where the thermocatalytic rate is slowest.
331 In the light assisted mode, the 2Ni catalyst produced syngas with the H_2/CO ratio of 0.61 and 0.47 at
332 460 and 362 °C, respectively. These values are substantially higher than the maximum values
333 predicted by the thermodynamic equilibrium. During thermally driven reaction at identical catalyst
334 temperatures, the H_2/CO ratio was 0.48 and 0.16. Consequently, light assisted DRM proceeds with
335 higher H_2 selectivity compared to thermocatalytic one at identical catalyst temperatures. The H_2
336 selectivity during DRM is strongly affected by the co-occurring RWGS reaction, and visible light
337 illumination diminishes its contribution to the product selectivity over Ni/CeO_{2-x} catalysts. This is in
338 line with previous findings of Zhou et al.[26], who attributed the 100 % H_2 selectivity during DRM to
339 visible light stimulating H_2 desorption from ruthenium active sites, thus decelerating the RWGS rate.
340 Long-term light assisted catalytic activity was tested at 400 °C for the most active 2Ni catalyst (Fig.
341 5D). During the 50 h time on stream, the initial CH_4 and CO_2 rates decreased by 37 and 35 %, and the
342 initial value of H_2/CO dropped from 0.55 to 0.44, revealing catalyst deactivation takes place. Analysis
343 of spent 2Ni catalyst identified only 1 wt. % of carbon on the sample, thus excluding active site
344 blocking as a source of deactivation.
345

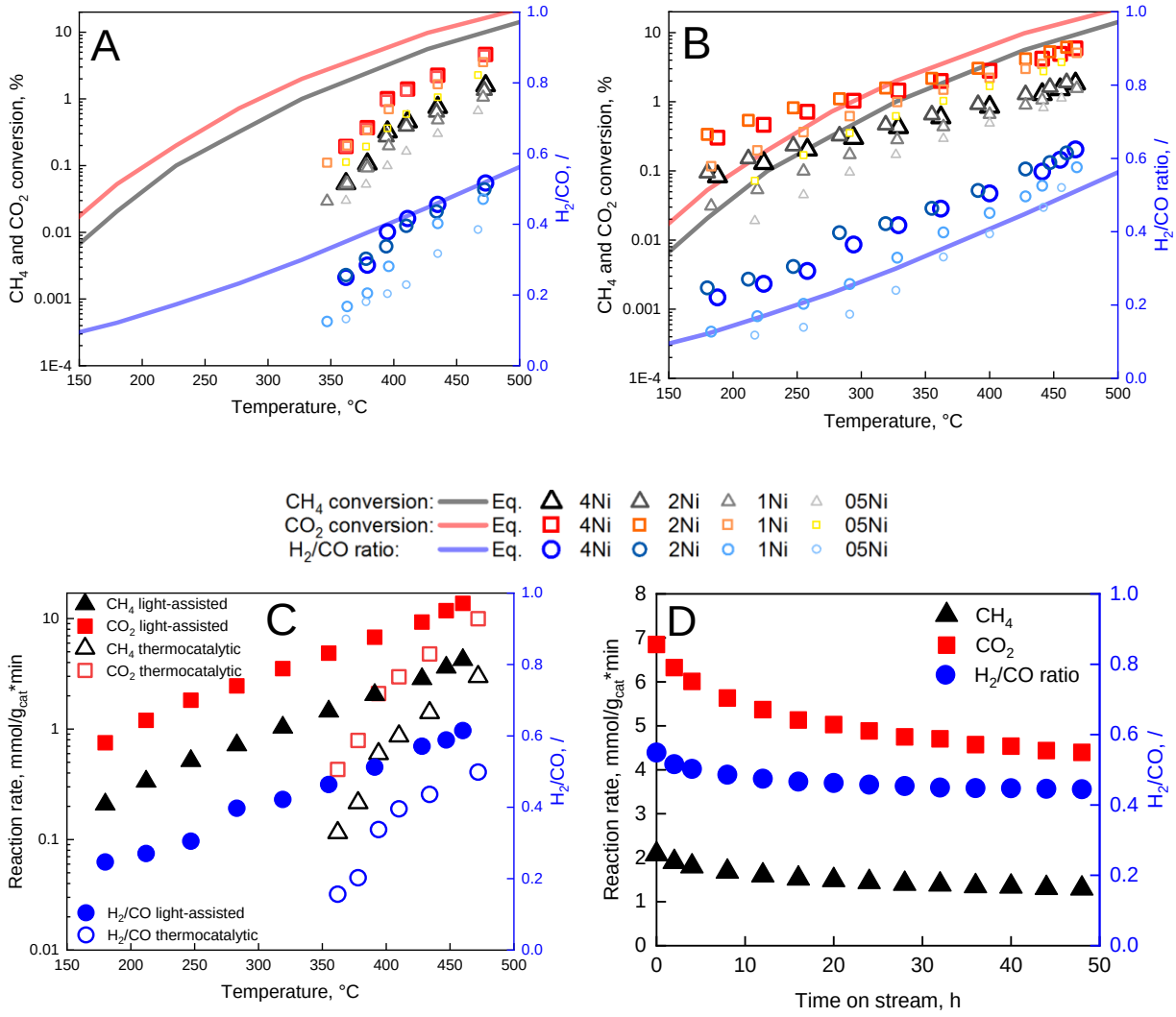

346 **Figure 5. (**A) Conversion of CH_4 and CO_2, as well as H_2/CO ratios produced during thermocatalytic and
347 (B) light-assisted DRM reaction over Ni/CeO_{2-x} nanorod catalysts. Thermodynamic equilibrium values
348 of CH_4 and CO_2 conversion and H_2/CO ratios are shown by full grey, red and blue lines. (C)
349 Comparison of CH_4 and CO_2 rates and H_2/CO ratio produced during light-assisted and thermocatalytic
350 DRM reaction over 2Ni catalyst as a function of catalyst temperature. (D) Long-term light assisted
351 performance of 2Ni catalyst at 400 °C and constant irradiation by 790 mW/cm^2 of white light.
352

353 The following analysis was applied to exclude the photo-thermal origin (sample heating) as the
354 source of the photocatalytic effect observed over Ni/CeO_{2-x} catalysts. The apparent activation
355 energies (Ea) in the thermocatalytic mode (90-130 kJ/mol) decreased to 30-55 kJ/mol in the light-
356 assisted mode (inset Figs. S11A and S12A). The apparent activation energy includes the contributions
357 of activation barriers for the rate-determining step (RDS), the enthalpy of the steps that produce
358 species involved in the RDS and a coverage-dependent contribution related to the enthalpy required

to regenerate the active sites occupied by reaction intermediates[44]. The observed strong decrease of Ea indicates a notable change in the reaction mechanism and a substantial alleviation of energy barriers related to the RDS (methane activation) by visible light.

Also, we estimated the local temperature increase of the 6 nm nickel particle under constant illumination as proposed by Baffou[45], which was found to be between 1 and 2 °C. The CH_4 rate is accelerated by about 5 % when the catalyst temperature increases by 2 °C. However, over the 2Ni sample, the smallest difference between light-assisted and thermally driven CH_4 rates was 71 % favouring light-assisted mode at identical catalyst temperature. Zhou et al.[26] compared the catalyst temperature upon visible light illumination in the same microreactor reactor as used in our work. The values measured by a thermocouple positioned in the catalyst bed and by the thermal camera were identical.

As a control experiment, light assisted DRM activity was benchmarked to the thermally driven over the $2Ni/SiO_2$ catalyst (Fig. S13). Silica is a wide bandgap insulator, and when coupled with poor visible light absorption of nickel (Fig. S10), negligible photocatalytic activity gain is expected during this experiment. Indeed, the CH_4 and CO_2 rates differ by less than 5 % in thermal and light-assisted DRM experiments at identical catalyst temperatures, revealing the temperature measurement inside the catalyst layer reflects the local temperature at the metallic particles. This experiment also confirmed that the accelerated DRM rate observed over Ni/CeO_2 catalysts is related to light absorption by the CeO_{2-x}, which agrees with our theoretical analysis (Figs. 3, S9 and S10). However, during the light-assisted DRM over $2Ni/SiO_2$, the H_2/CO ratio was consistently higher compared to the thermocatalytic experiment. This is likely a result of accelerated H_2 desorption from the nickel surface via desorption induced by electronic transitions (DIET) mechanism[46], which decelerated the RWGS reaction rate. Control experiments with pure CeO_2-R support and SiC confirmed their negligible contribution to photocatalytic activity and identified the presence of nickel as crucial for enabling the DRM reaction (Fig. S14). Based on the above, we can confidently assign the observed DRM rate acceleration upon illumination has a photocatalytic and not photo-thermal origin.

The effect of wavelength on light-assisted DRM activity was tested on the 2Ni catalyst at a constant irradiance of 300 mW/cm^2 using different bandpass filters (Fig. 6A). The acceleration of CH_4 rate was observed for all wavelengths, compared to the thermally driven methane rate, which equalled 0.49 $mmol/g_{cat}$*min at identical catalyst temperature. Interestingly, the lowest light assisted CH_4 rate (0.61 $mmol/g_{cat}$*min) was observed for illumination with wavelengths shorter than 450 nm, which is the only fraction of light that enables electron promotion from the VB to the CB of CeO_{2-x} and their further migration to nickel nanoparticles, where they can assist in methane activation. The methane rate of 0.62 $mmol/g_{cat}$*min was achieved during illumination with the lowest energy photons ($\lambda >$ 600 nm), which can undergo only sub-bandgap electron transitions. The most pronounced rate

acceleration was observed with wavelengths between 400 and 500 nm, which correlates with the wavelength dependence of the near field electromagnetic intensity enhancement on nickel nanoparticles (Fig. 3C).

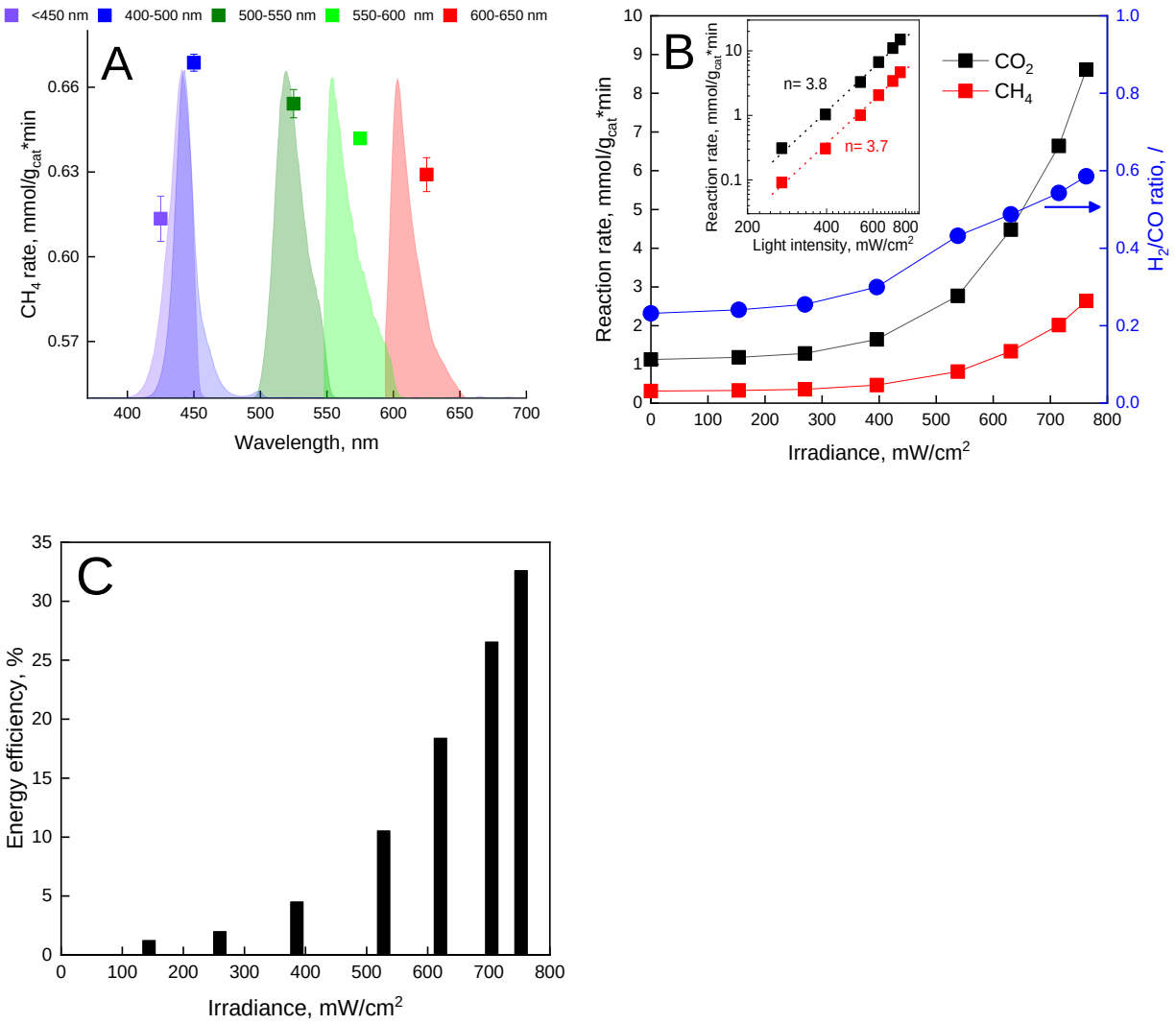

Figure 6. (A) The CH_4 rate as a function of wavelength at constant irradiance of 300 mW/cm^2 and constant catalyst temperature of 395 °C. Coloured cones show light intensity dependence on wavelength when using different bandpass filters. (B) CH_4 and CO_2 rate with corresponding H_2/CO ratio as a function of irradiance at a constant catalyst temperature of 400 °C. (C) Energy efficiency related to the experiment shown in (B).

The effect of irradiance on the CH_4 and CO_2 rates, as well as H_2/CO ratio over the 2Ni catalyst, was probed at the constant catalyst temperature of 400 °C (Fig. 6B). The study of the influence of light intensity on the photocatalytic rate is a powerful tool to analyze the reaction mechanisms in light assisted reactions.[47] Four different kinetic categories for the light intensity (I) dependence on the

photocatalytic reaction rate are classified: sublinear (rate $\propto I^n$, n<1), linear (rate $\propto$ I), superlinear (rate $\propto I^n$, n>1) and exponential (rate $\propto e^{f(I)}$).[48] Plasmon-induced photocatalysis has been demonstrated to exhibit each ofthese regimes depending on the operating conditions, except for the sublinear dependence, which is characteristic of non-plasmonic semiconductor catalysis when charge carrier recombination is dominant.[49] An exponential dependence of the reaction rate on illumination intensity is characteristic of thermally driven transformations. A first order relationship between the photon flux and reaction rate implies that a single photon absorption induces the chemical reaction. Both linear (rate $\propto$ I) and superlinear (rate $\propto I^n$, n>1) regimes are distinctive features of electron-driven chemical transformations on metal surfaces, but the reaction conditions are the key factor determining the prevalence of each of them.[47]

The acceleration of CH_4 and CO_2 rates, as well as H_2/CO ratio, started to increase notably as irradiance exceeded 400 mW/cm^2. At 790 mW/cm^2, the CH_4 and CO_2 rates were accelerated by 852 and 769 % compared to the thermocatalytic experiment in the dark at identical catalyst temperature, and the H_2/CO ratio increased from 0.23 to 0.59. The inset in Fig. 6B shows the superlinear depencence of both CH_4 and CO_2 rates on irradiance over 2Ni/CO_{2-x} catalysts. This again points to a conclusion that electron-driven chemical transformations on metal surfaces and not thermal energy are responsible for rate acceleration.

The calculated energy efficiency (Fig. 6C) increased rapidly at irradiances above 400 mW/cm^2 and reached 33 % at 790 mW/cm^2. This revealed the 2Ni as an efficient photocatalyst for visible light utilisation.

Hot carriers generated by plasmon decay in the nickel nanoparticles were analyzed by DFT, as they could alter the reaction pathway of methane dissociation. Initial hot carrier probability distribution can be obtained from calculated density of states (DOS, see supplementary information and Fig. S15) for photoexcitation with energy E_{ph} and Fermi distribution at room temperature. Probability distributions for hot carrier generation obtained in that way (Figure S16) suggest that, for photon energies corresponding to visible light (up to 3.26 eV or 380 nm), Ni should not be an efficient source of hot carriers.

Cumulative hot carrier generation probability (Figure S17) shows that the probability for hot carrier generation increases graudally and almost linearly with the increasing photon energy in the visible range, after which it sharply increases in the UV. In contrast, the experimental data presented in Fig. 6A shows a sharp decrease of reaction rate below 450 nm (above 2.76 eV). Had the reaction been catalyzed by hot carriers generated in Ni nanoparticles, the reaction rate would be expected to follow the trend of hot carrier generation probability and continue increasing as the wavelength gets shorter. It has to be noted that hot carrier generation probability is an intrinsic property of the material and the near-field intensity could change the absolute number of generated hot carriers

and, consequently, the rate of reaction catalyzed by hot carriers. Keeping near-field intensity in mind, the possibility of a significant influence of hot carrier generation in Ni on the reaction rate can not be discarded by diverging trends alone but, as can be seen on Figure 4, the near-field intensity enhancement is relatively poor inside the Ni nanoparticles, which also does not go in favor of hot carrier generation. The aforementioned observations – unremarkable hot carrier generation probability in the spectral range the experiments were carried in, diverging trends in generation probability and reaction rate as the photon energy approaches UV, and low near-field intensity enhancement inside Ni nanoparticles – suggest the hot carriers are unlikely to be generated in Ni nanoparticles.

Based on the characterisation, theoretical and catalytic data presented above, we can postulate the light assisted DRM mechanism over Ni/CeO_{2-x} catalysts. During DRM reaction, nickel is present as metallic nanoparticles[35] measuring about 5 nm and ceria as a partly reduced (CeO_{2-x}) semiconductor oxide [35]. Ceria is an n-type semiconductor whose work function (5.34 eV) is larger than that of nickel (5.01 eV).[50] After illuminating the Ni/CeO_{2-x} catalysts with photons having energy higher than the absorption edge of ceria (λ<450 nm), the photoexcited electrons migrate from the VB to CB of ceria and are transferred to nickel. An upward band bending in the n-type semiconductor is created due to the accumulation of excess positive charge in the semiconductor caused by electron migration. As a result, a Schottky barrier is created, which serves as an electron trap leading to electron accumulation on the nickel and prevents the migration of electrons back to the semiconductor. The electrons from nickel can be transferred to the LUMO of adsorbed methane and electronically excite the CH_x species, accelerating the C-H bond cleavage and dehydrogenation. Illumination by 300 mW/cm^2 of light with λ<450 nm resulted in a methane rate of 0.61 $mmol/g_{cat}$*min, compared to 0.49 $mmol/g_{cat}$*min in the dark at identical catalyst temperature, which represents a 24 % rate acceleration.

However, since the light-assisted rate acceleration does not correlate with decreasing wavelength (increasing photon energy), this photocatalytic mechanism is not dominant in the case studied. Namely, photons with a shorter wavelength can excite electrons to higher energy levels in the conduction band (CB), increasing the overpotential for charge carriers and thus increasing their reactivity. Furthermore, the methane rate, achieved by illuminating with photons having substantially lower energy than required for VB to CB transition in ceria, is higher compared to the methane rate achieved by photons with sufficient energy that enable bandgap transitions (Fig. 6A). This suggests the existence of an additional light-driven reaction mechanism. The near-field electromagnetic enhancement is strongly dependent on the illumination wavelength and reaches a maximum at about 500 nm. Upon illuminating the 2Ni catalyst with 300 mW/cm^2 of light using a bandpass filter transparent for wavelengths between 500 and 550 nm, a methane rate of 0.65

mmol/g_{cat}*min was achieved which represents a 33 % increase compared to the experiment in the dark. Consequently, the contribution of near field enhancement on methane rate acceleration outweighs the contribution from photocatalytic interphase charge transfer. The highest near field enhancement (more than 80 times compared to the incident irradiation, Fig. 3C) occurs over the nickel surface and the nickel-ceria interface, which are the active sites for the rate-determining methane activation step in the DRM reaction. The oscillations of excited electrons on the surface of nickel can induce multiple vibrational transitions of the Ni-CH_x bond, and as the vibrational energy stored in the bond increases, it gets progressively more destabilised.[51] As a result, the energy barriers related to methane dissociation are lowered, which manifests macroscopically as accelerated methane rate. Consequently, near field enhancement appears as a dominant source of rate acceleration during light-assisted DRM over Ni/CeO_{2-x} catalyst.

Conclusions

This work analyses the underlying mechanism of visible light assisted DRM rate acceleration over Ni/CeO_{2-x} catalysts. The *in-situ* UV-Vis analysis and simulation of electromagnetic properties revealed that the presence of Ce^{3+} in partly reduced ceria is crucial for visible light absorption. The light-assisted DRM test showed that methane and CO_2 rates, as well as hydrogen selectivity, are greatly improved compared to thermally driven experiments at identical catalyst temperatures. Two weight percent nickel was found as optimal active metal loading, enabling high (photocatalytic) reaction rates,energy efficiency of 33 % and minimal carbon accumulation. Photocatalytic DRM activity is maintained over the 2Ni catalyst in purely photocatalytic mode with 790 mW/cm^2 of white light irradiance and without external heating. Simulation of electromagnetic properties identified the electromagnetic near field intensity enhancement occurs mainly over nickel nanoparticles, which are the active sites for methane activation. The light assisted DRM rate is wavelength dependent and reaches a maximum at about 500 nm, which also triggers the highest near field enhancement. Two mechanisms exist simultaneously during white light illumination: photocatalytic interphase charge transfer employing photons with energy higher than the bandgap of partly reduced ceria and near field enhancement over nickel nanoparticles, stimulated by sub- bandgap absorption of low energy photons. This work can act as a cornerstone for further developing Ni/CeO_2 based catalysts for visible light-driven methane activation under mild conditions.

Acknowledgements:

PD, KL and MM acknowledge Slovenian Research Agency (ARRS) for financial support through programs P2-150, P1-0021 and project J2-1726 *˝Thermocatalytic and combined thermo-photocatalytic CH_4 reforming with CO_2 over nanoshaped Ni/CeO_2 and PM-Ni/CeO_2-TiO_2 materials˝*. JZ

acknowledges the support from the European Union's Horizon 2020 research and innovation program under grant agreement No. 823717 - ESTEEM3. JS and MB acknowledge the finantial support of the Croatian Science Foundation thorugh the grant number IP-2019-04-5424.

References

(1) Saeidi, S.; Amin, N. A. S.; Rahimpour, M. R. Hydrogenation of CO2 to Value-Added Products—A Review and Potential Future Developments. *J. CO2 Util.* **2014**, *5*, 66–81.

(2) Chang, K.; Zhang, H.; Cheng, M.; Lu, Q. Application of Ceria in CO2 Conversion Catalysis. *ACS Catal.* **2020**, *10* (1), 613–631.

(3) Indarto, A.; Palgunadi, J. *Syngas: Production, Applications and Environmental Impact*; Nova Science Publishers, Inc., 2013.

(4) Pakhare, D.; Spivey, J. A Review of Dry (CO2) Reforming of Methane over Noble Metal Catalysts. *Chem. Soc. Rev.* **2014**, *43* (22), 7813–7837.

(5) Horn, R.; Schlögl, R. Methane Activation by Heterogeneous Catalysis. *Catal. Letters* **2015**, *145* (1), 23–39.

(6) Lustemberg, P. G.; Ramírez, P. J.; Liu, Z.; Gutiérrez, R. A.; Grinter, D. G.; Carrasco, J.; Senanayake, S. D.; Rodriguez, J. A.; Ganduglia-Pirovano, M. V. Room-Temperature Activation of Methane and Dry Reforming with CO2 on Ni-CeO2 (111) Surfaces: Effect of Ce3+ Sites and Metal–Support Interactions on C–H Bond Cleavage. *ACS Catal.* **2016**, *6* (12), 8184–8191.

(7) Zhang, F.; Liu, Z.; Chen, X.; Rui, N.; Betancourt, L. E.; Lin, L.; Xu, W.; Sun, C.-J.; Abeykoon, A. M. M.; Rodriguez, J. A.; et al. The Effects of Zr-Doping into Ceria for the Dry Reforming of Methane over Ni/CeZrO2 Catalysts: In-Situ Studies with XRD, XAFS and AP-XPS. *ACS Catal.* **2020**, acscatal.9b04451.

(8) Vogt, C.; Kranenborg, J.; Monai, M.; Weckhuysen, B. M. Structure Sensitivity in Steam and Dry Methane Reforming over Nickel: Activity and Carbon Formation. *ACS Catal.* **2020**, *10* (2), 1428–1438.

(9) Pakhare, D.; Spivey, J. A Review of Dry (CO 2) Reforming of Methane over Noble Metal Catalysts. *Chem. Soc. Rev.* **2014**, *43* (22), 7813–7837.

(10) Trovarelli, A. *Catalysis by Ceria and Related Materials*; Catalytic Science Series; PUBLISHED BY IMPERIAL COLLEGE PRESS AND DISTRIBUTED BY WORLD SCIENTIFIC PUBLISHING CO., 2002; Vol. 2.

(11) Djinović, P.; Osojnik Črnivec, I. G.; Erjavec, B.; Pintar, A. Influence of Active Metal Loading and Oxygen Mobility on Coke-Free Dry Reforming of Ni–Co Bimetallic Catalysts. *Appl. Catal. B Environ.* **2012**, *125*, 259–270.

(12) Djinović, P.; Pintar, A. Stable and Selective Syngas Production from Dry CH 4 -CO 2 Streams

548 over Supported Bimetallic Transition Metal Catalysts. *Appl. Catal. B Environ.* **2017**, *206*, 675–
549 682.
550 (13) Trovarelli, A.; Llorca, J. Ceria Catalysts at Nanoscale: How Do Crystal Shapes Shape Catalysis?
551 *ACS Catal.* **2017**, *7* (7), 4716–4735.
552 (14) Chang, K.; Zhang, H.; Cheng, M.; Lu, Q. Application of Ceria in CO 2 Conversion Catalysis. *ACS*
553 *Catal.* **2020**, *10* (1), 613–631.
554 (15) Du, X.; Zhang, D.; Shi, L.; Gao, R.; Zhang, J. Morphology Dependence of Catalytic Properties of
555 Ni/CeO 2 Nanostructures for Carbon Dioxide Reforming of Methane. *J. Phys. Chem. C* **2012**,
556 *116* (18), 10009–10016.
557 (16) Palmisano, G.; Augugliaro, V.; Pagliaro, M.; Palmisano, L. Photocatalysis: A Promising Route
558 for 21st Century Organic Chemistry. *Chem. Commun.* **2007**, No. 33, 3425.
559 (17) Neațu, Ștefan; Maciá-Agulló, J.; Garcia, H. Solar Light Photocatalytic CO2 Reduction: General
560 Considerations and Selected Bench-Mark Photocatalysts. *Int. J. Mol. Sci.* **2014**, *15* (4), 5246–
561 5262.
562 (18) Chen, L.; Tang, J.; Song, L.-N.; Chen, P.; He, J.; Au, C.-T.; Yin, S.-F. Heterogeneous
563 Photocatalysis for Selective Oxidation of Alcohols and Hydrocarbons. *Appl. Catal. B Environ.*
564 **2019**, *242*, 379–388.
565 (19) Shoji, S.; Peng, X.; Yamaguchi, A.; Watanabe, R.; Fukuhara, C.; Cho, Y.; Yamamoto, T.;
566 Matsumura, S.; Yu, M.-W.; Ishii, S.; et al. Photocatalytic Uphill Conversion of Natural Gas
567 beyond the Limitation of Thermal Reaction Systems. *Nat. Catal.* **2020**, *3* (2), 148–153.
568 (20) Mehta, P.; Barboun, P. M.; Engelmann, Y.; Go, D. B.; Bogaerts, A.; Schneider, W. F.; Hicks, J. C.
569 Plasma-Catalytic Ammonia Synthesis beyond the Equilibrium Limit. *ACS Catal.* **2020**, *10* (12),
570 6726–6734.
571 (21) Song, H.; Meng, X.; Dao, T. D.; Zhou, W.; Liu, H.; Shi, L.; Zhang, H.; Nagao, T.; Kako, T.; Ye, J.
572 Light-Enhanced Carbon Dioxide Activation and Conversion by Effective Plasmonic Coupling
573 Effect of Pt and Au Nanoparticles. *ACS Appl. Mater. Interfaces* **2018**, *10* (1), 408–416.
574 (22) Han, B.; Wei, W.; Chang, L.; Cheng, P.; Hu, Y. H. Efficient Visible Light Photocatalytic CO2
575 Reforming of CH4. *ACS Catal.* **2016**, *6* (2), 494–497.
576 (23) Liu, H.; Li, M.; Dao, T. D.; Liu, Y.; Zhou, W.; Liu, L.; Meng, X.; Nagao, T.; Ye, J. Design of PdAu
577 Alloy Plasmonic Nanoparticles for Improved Catalytic Performance in CO2 Reduction with
578 Visible Light Irradiation. *Nano Energy* **2016**, *26*, 398–404.
579 (24) Cho, Y.; Shoji, S.; Yamaguchi, A.; Hoshina, T.; Fujita, T.; Abe, H.; Miyauchi, M. Visible-Light-
580 Driven Dry Reforming of Methane Using a Semiconductor-Supported Catalyst. *Chem.*
581 *Commun.* **2020**, *56* (33), 4611–4614.
582 (25) Abdel Karim Aramouni, N.; Zeaiter, J.; Kwapinski, W.; Ahmad, M. N. Thermodynamic Analysis

583 of Methane Dry Reforming: Effect of the Catalyst Particle Size on Carbon Formation. *Energy*
584 *Convers. Manag.* **2017**, *150* (March), 614–622.
585 (26) Zhou, L.; Martirez, J. M. P.; Finzel, J.; Zhang, C.; Swearer, D. F.; Tian, S.; Robatjazi, H.; Lou, M.;
586 Dong, L.; Henderson, L.; et al. Light-Driven Methane Dry Reforming with Single Atomic Site
587 Antenna-Reactor Plasmonic Photocatalysts. *Nat. Energy* **2020**, *5* (1), 61–70.
588 (27) Khan, M. E.; Khan, M. M.; Cho, M. H. Ce3+-Ion, Surface Oxygen Vacancy, and Visible Light-
589 Induced Photocatalytic Dye Degradation and Photocapacitive Performance of CeO2-Graphene
590 Nanostructures. *Sci. Rep.* **2017**, *7* (1), 5928.
591 (28) Zabilskiy, M.; Djinović, P.; Tchernychova, E.; Tkachenko, O. P.; Kustov, L. M.; Pintar, A.
592 Nanoshaped CuO/CeO 2 Materials: Effect of the Exposed Ceria Surfaces on Catalytic Activity in
593 N 2 O Decomposition Reaction. *ACS Catal.* **2015**, *5* (9), 5357–5365.
594 (29) Słowik, G.; Greluk, M.; Rotko, M.; Machocki, A. Evolution of the Structure of Unpromoted and
595 Potassium-Promoted Ceria-Supported Nickel Catalysts in the Steam Reforming of Ethanol.
596 *Appl. Catal. B Environ.* **2018**, *221* (May 2017), 490–509.
597 (30) Velu, S.; Gangwal, S. Synthesis of Alumina Supported Nickel Nanoparticle Catalysts and
598 Evaluation of Nickel Metal Dispersions by Temperature Programmed Desorption. *Solid State*
599 *Ionics* **2006**, *177* (7–8), 803–811.
600 (31) Hohenester, U.; Trügler, A. MNPBEM – A Matlab Toolbox for the Simulation of Plasmonic
601 Nanoparticles. *Comput. Phys. Commun.* **2012**, *183* (2), 370–381.
602 (32) *Handbook of Optical Constants of Solids*; Palik, E. D., Ed.; Academic press, 1998.
603 (33) Wheeler, V. M.; Zapata, J. I.; Kreider, P. B.; Lipiński, W. Effect of Non-Stoichiometry on Optical,
604 Radiative, and Thermal Characteristics of Ceria Undergoing Reduction. *Opt. Express* **2018**, *26*
605 (10), A360.
606 (34) Djinović, P.; Pintar, A. Stable and Selective Syngas Production from Dry CH4-CO2 Streams over
607 Supported Bimetallic Transition Metal Catalysts. *Appl. Catal. B Environ.* **2017**, *206*, 675–682.
608 (35) Zhang, F.; Liu, Z.; Chen, X.; Rui, N.; Betancourt, L. E.; Lin, L.; Xu, W.; Sun, C.-J.; Abeykoon, A. M.
609 M.; Rodriguez, J. A.; et al. Effects of Zr Doping into Ceria for the Dry Reforming of Methane
610 over Ni/CeZrO 2 Catalysts: In Situ Studies with XRD, XAFS, and AP-XPS. *ACS Catal.* **2020**, 3274–
611 3284.
612 (36) Marabelli, F.; Wachter, P. Covalent Insulator CeO2: Optical Reflectivity Measurements. *Phys.*
613 *Rev. B* **1987**, *36* (2), 1238–1243.
614 (37) Zabilskiy, M.; Djinović, P.; Tchernychova, E.; Pintar, A. N 2 O Decomposition over CuO/CeO 2
615 Catalyst: New Insights into Reaction Mechanism and Inhibiting Action of H 2 O and NO by
616 Operando Techniques. *Appl. Catal. B Environ.* **2016**, *197*, 146–158.
617 (38) Amekura, H.; Takeda, Y.; Kishimoto, N. Criteria for Surface Plasmon Resonance Energy of

618 Metal Nanoparticles in Silica Glass. *Nucl. Instruments Methods Phys. Res. Sect. B Beam*
619 *Interact. with Mater. Atoms* **2004**, *222* (1–2), 96–104.
620 (39) Zuloaga, J.; Nordlander, P. On the Energy Shift between Near-Field and Far-Field Peak
621 Intensities in Localized Plasmon Systems. *Nano Lett.* **2011**, *11* (3), 1280–1283.
622 (40) Sergiienko, S.; Moor, K.; Gudun, K.; Yelemessova, Z.; Bukasov, R. Nanoparticle–Nanoparticle
623 vs. Nanoparticle–Substrate Hot Spot Contributions to the SERS Signal: Studying Raman
624 Labelled Monomers, Dimers and Trimers. *Phys. Chem. Chem. Phys.* **2017**, *19* (6), 4478–4487.
625 (41) Liu, Z.; Grinter, D. C.; Lustemberg, P. G.; Nguyen-Phan, T.-D.; Zhou, Y.; Luo, S.; Waluyo, I.;
626 Crumlin, E. J.; Stacchiola, D. J.; Zhou, J.; et al. Dry Reforming of Methane on a Highly-Active Ni-
627 CeO 2 Catalyst: Effects of Metal-Support Interactions on C−H Bond Breaking. *Angew. Chemie*
628 *Int. Ed.* **2016**, *55* (26), 7455–7459.
629 (42) Xie, Z.; Liao, Q.; Liu, M.; Yang, Z.; Zhang, L. Micro-Kinetic Modeling Study of Dry Reforming of
630 Methane over the Ni-Based Catalyst. *Energy Convers. Manag.* **2017**, *153* (August), 526–537.
631 (43) Yuan, K.; Zhong, J.-Q.; Zhou, X.; Xu, L.; Bergman, S. L.; Wu, K.; Xu, G. Q.; Bernasek, S. L.; Li, H.
632 X.; Chen, W. Dynamic Oxygen on Surface: Catalytic Intermediate and Coking Barrier in the
633 Modeled CO 2 Reforming of CH 4 on Ni (111). *ACS Catal.* **2016**, *6* (7), 4330–4339.
634 (44) Lynggaard, H.; Andreasen, A.; Stegelmann, C.; Stoltze, P. Analysis of Simple Kinetic Models in
635 Heterogeneous Catalysis. *Prog. Surf. Sci.* **2004**, *77* (3–4), 71–137.
636 (45) Baffou, G.; Rigneault, H. Femtosecond-Pulsed Optical Heating of Gold Nanoparticles. *Phys.*
637 *Rev. B* **2011**, *84* (3), 035415.
638 (46) Ageev, V. N. Desorption Induced by Electronic Transitions. *Prog. Surf. Sci.* **1994**, *47* (1–2), 55–
639 203.
640 (47) Mateo, D.; Cerrillo, J. L.; Durini, S.; Gascon, J. Fundamentals and Applications of Photo-
641 Thermal Catalysis. *Chem. Soc. Rev.* **2021**, *50*, 2173–2210.
642 (48) Kale, M. J.; Avanesian, T.; Christopher, P. Direct Photocatalysis by Plasmonic Nanostructures.
643 *ACS Catal.* **2014**, *4* (1), 116–128.
644 (49) Gellé, A.; Jin, T.; de la Garza, L.; Price, G. D.; Besteiro, L. V.; Moores, A. Applications of
645 Plasmon-Enhanced Nanocatalysis to Organic Transformations. *Chem. Rev.* **2020**, *120* (2), 986–
646 1041.
647 (50) Zhao, K.; Qi, J.; Yin, H.; Wang, Z.; Zhao, S.; Ma, X.; Wan, J.; Chang, L.; Gao, Y.; Yu, R.; et al.
648 Efficient Water Oxidation under Visible Light by Tuning Surface Defects on Ceria Nanorods. *J.*
649 *Mater. Chem. A* **2015**, *3* (41), 20465–20470.
650 (51) Zhou, L.; Swearer, D. F.; Robatjazi, H.; Alabastri, A.; Christopher, P.; Carter, E. A.; Nordlander,
651 P.; Halas, N. J. Response to Comment on “Quantifying Hot Carrier and Thermal Contributions
652 in Plasmonic Photocatalysis.” *Science (80-.).* **2019**, *364* (6439), 69–72.

Supplementary information for

On the mechanism of visible-light accelerated methane dry reforming reaction over Ni/CeO_{2-x} catalysts

Kristijan Lorber[1,3], Janez Zavašnik[2], Jordi Sancho-Parramon[4], Matej Bubaš[4], Matjaž Mazaj[1] and Petar Djinović[1,3]*

[1]Department of Inorganic Chemistry and Technology, National Institute of Chemistry, Hajdrihova 19, SI-1000 Ljubljana, Slovenia

[2]Jožef Stefan Institute, Jamova cesta 39, SI-1000 Ljubljana, Slovenia

[3]University of Nova Gorica, Vipavska 13, SI-5000 Nova Gorica, Slovenia

[4]Ruđer Bošković Institute, Division of Materials Physics, Bijenička cesta 54, 10000 Zagreb, Croatia

*corresponding author e-mail: petar.djinovic@ki.si

Contents:

Calculating CH_4 and CO_2 reaction rates, H_2/CO ratio and energy efficiency of the light assisted reaction

The rates of H_2 (rH_2) and CO (rCO) formation were calculated according to Equation 1:

$$(H_2) = cH_2(\%) \cdot f_{out}(\text{ml/min})/22414(ml/mol) \quad (1)$$

In Equation 1, cH_2 is the concentration of product (H_2, as obtained from calibrated GC analysis of gas stream exiting the reactor), $_{out}$ is the volumetric flow rate of the gas exiting the reactor. The expansion of gas volume as a result of DRM reaction stoichiometry (2mol → 4mol, see Equation 2) was neglected due to low methane and CO_2 conversions achieved during catalytic tests (below 2%). The CO formation rate was calculated identical as above, only CO concentration was used instead of H_2.
The rate of CH_4 (rCH_4) and CO_2 (rCO_2) conversion are usually calculated directly from gas phase analysis and gas flow rates. In this particular case where conversions below 2% were achieved, the relative uncertainty of GC analysis (about 1% RSD) would induce errors far greater than the actual catalytic activity. As a result, CH_4 and CO_2 rates (rCH_4) and $r(CO_2)$, respectively, were calculated from H_2 and CO formation rates considering the contribution of DRM (Equation 2) and RWGS (Equation 3) reactions.

$$CH_4 + CO_2 \leftrightarrow 2H_2 + 2CO \quad (2)$$
-x -x 2x 2x

$$CO_2 + H_2 \leftrightarrow CO + H_2O \quad (3)$$
-y -y y y

By combining $(H_2) = 2x - y$, $(CO) = 2x + y$ and $(H_2O) = y$, we can calculate the individual rates as:

$$r(CH_4) = \frac{r(H_2)+r(CO)}{4} \quad (4)$$

$$r(CO_2) = \frac{r(H_2)}{2} + r(CO) \quad (5)$$

$$r(H_2O) = \frac{r(CO)-r(H_2)}{2} \quad (6)$$

The H_2/CO ratio reflects the selectivity of catalysts and is expressed as:

$$H_2/CO = r(H_2)/r(CO) \quad (7)$$

The energy efficiency of light assisted DRM reaction was calculated as follows:

$$\eta = \frac{a*\Delta H^0_{DRM} + b*\Delta H^0_{RWGS}}{light\ power} * 100\ \%$$

a (mol/s)= moles of methane converted per second
b (mol/s)= moles of water produced per second

The values a and b are calculated by subtracting the methane rate in thermocatalytic mode from the methane rate in light assisted mode at identical catalyst temperature.

Where ΔH^0_{DRM} =247 kJ/mol and ΔH^0_{RWGS}= 41 kJ/mol are the standard reaction enthalpy changes of the MDR and RWGS reactions.
Light power is the power emitted by the LED source (J/s).

Table S 1. Structural properties obtained by N_2 physisorption analysis of CeO_2 nanorod support and

Ni/CeO_2catalysts containing 0.5-4 wt. % nickel.

Sample	S_{BET}, m^2/g	V_{PORE}, cm^3/g	d_{PORE}, nm
CeO_2-R	84	0.24	11
05Ni-R	89	0.39	16
1Ni-R	87	0.29	13
2Ni-R	84	0.28	13
4Ni-R	80	0.34	16

Table S 2. Average nickel particle size, hydrogen consumed for sample reduction during H_2-TPR and fraction of Ce^{3+} achieved and amount of carbon accumulated during DRM tests.

Sample	Nickel particle size, nm[a]	H_2 consumed, mmol/g[b]	Carbon accumulated, wt. %
CeO_2	/	0.50 (17)	/
1Ni	5.4±1.4	0.71 (19)	0.2
2Ni	5.1±2.0 (4.8)	0.83 (17)	0.2
4Ni	6.5±1.7 (5.2)	0.92 (9)	12

[a]Measured and calculated from TEM micrographs. Values in parentheses were obtained from H_2 chemisorption-TPD data.

[b]Values in parentheses represent a fraction of Ce^{3+} achieved during H_2-TPR at 550 °C.

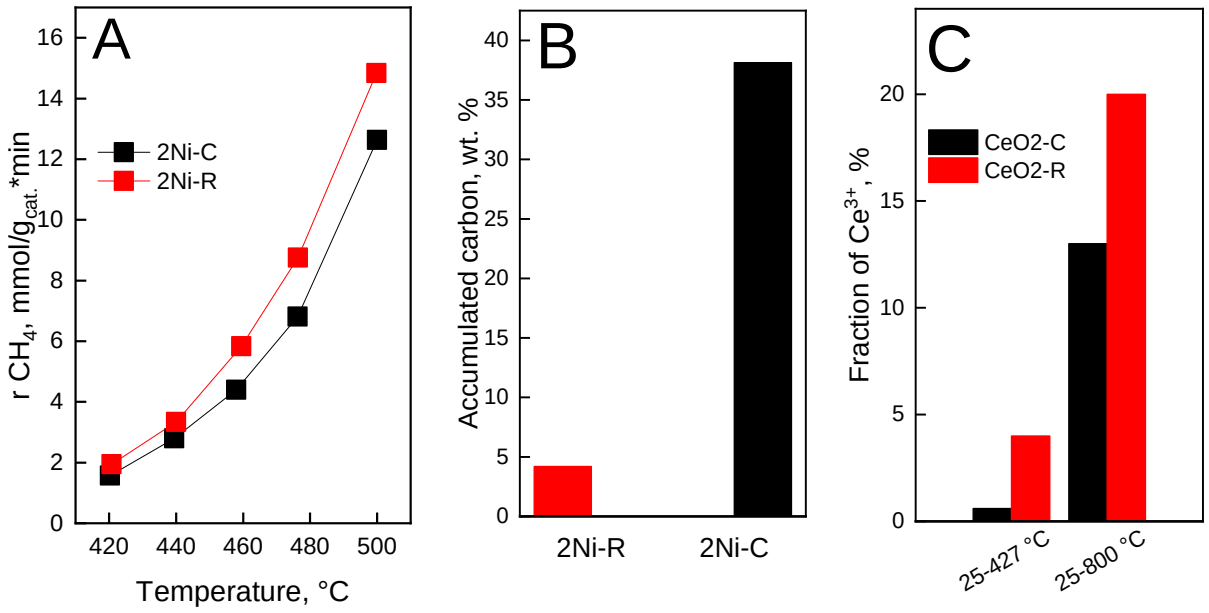

Figure S 1. (A) Methane reaction rate during DRM for catalysts containing 2 wt. % nickel dispersed on nanorods (2Ni-R) and nanocubes (2Ni-C),(B) amounts of accumulated carbon during 6 h of DRM reaction at 500 °C, CH_4=CO_2= 10 ml/min, 20 mg of catalyst and (C) fraction of Ce^{3+} achieved during H_2-TPR analysis of CeO_2-C and CeO_2-R supports between 25 and 427 °C or between 25 and 800 °C.

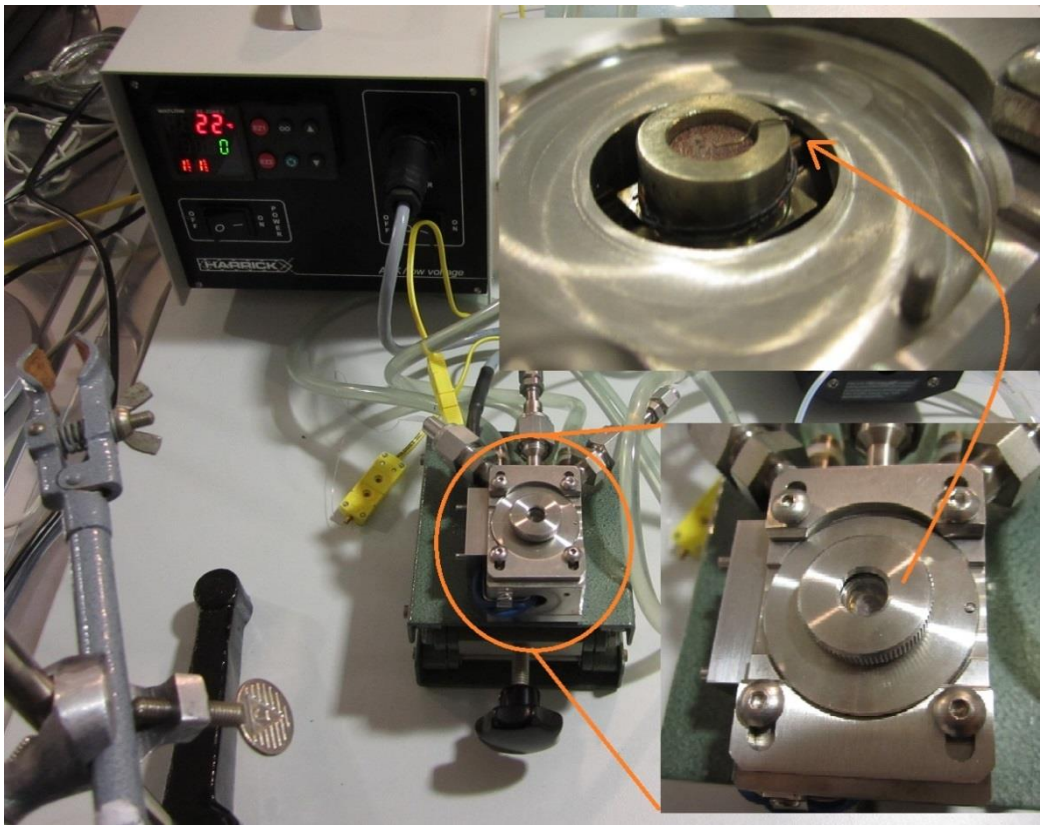

744

745 **Figure S 2.**The modified Harrick HVC-MRA reaction chamber used for thermocatalytic and light
746 assisted catalytic experiments.
747

748

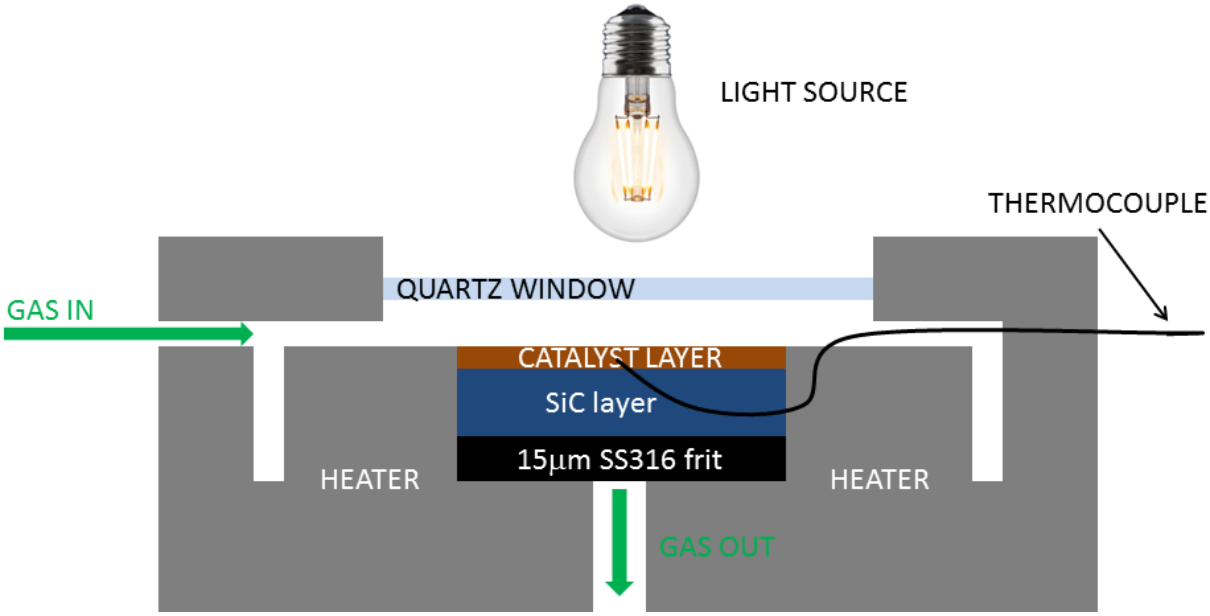

749

750 **Figure S 3.** Graphical representation of the reaction chamber (side view).

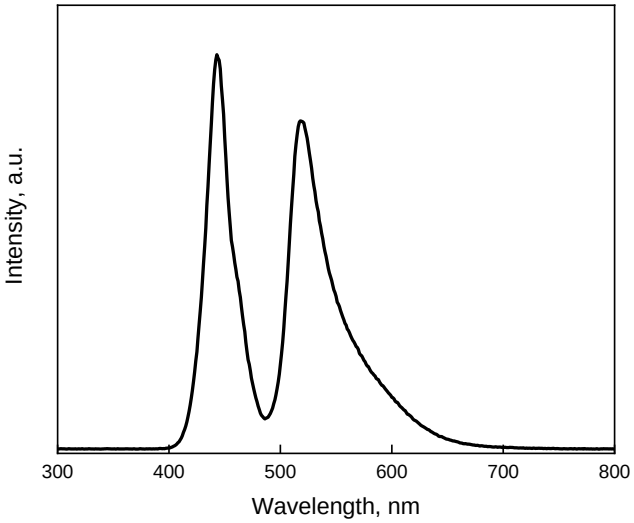

751

752 **Figure S 4.** The emission spectrum of the LED source used in the light assisted DRM experiments.

753

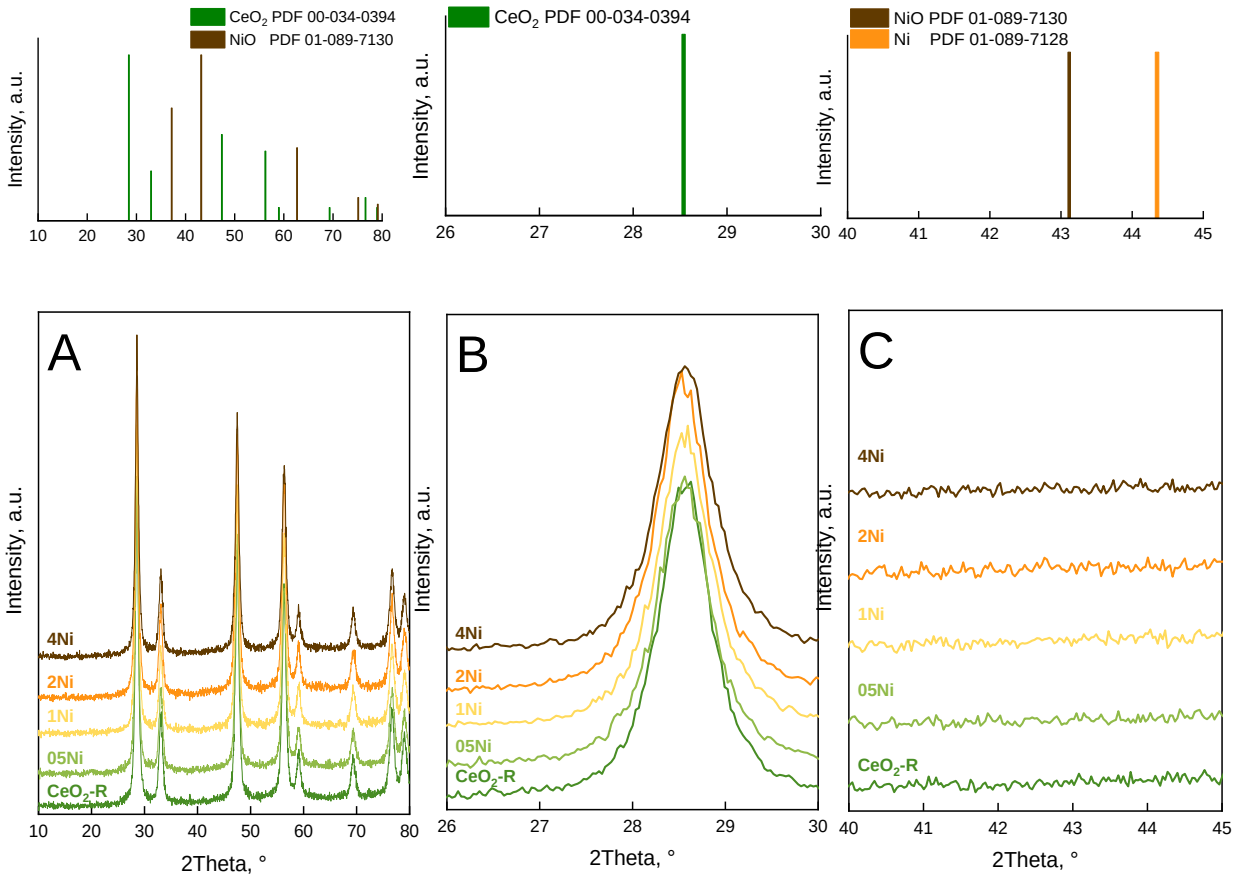

754 **Figure S 5**. (A)XRD diffraction patterns of bare CeO_2 nanorods and Ni/CeO_2 catalysts containing 0-4
755 wt. % nickel, (B) magnification of the CeO_2 [111] peak region and (C) magnification of the 2theta
756 region where the most intensive diffraction from NiO[200] and Ni[111] (both cubic, Fm-3m phase) is
757 expected. The upper panel shows expected peak positions based on diffraction CeO_2, NiO and Ni
758 standards.

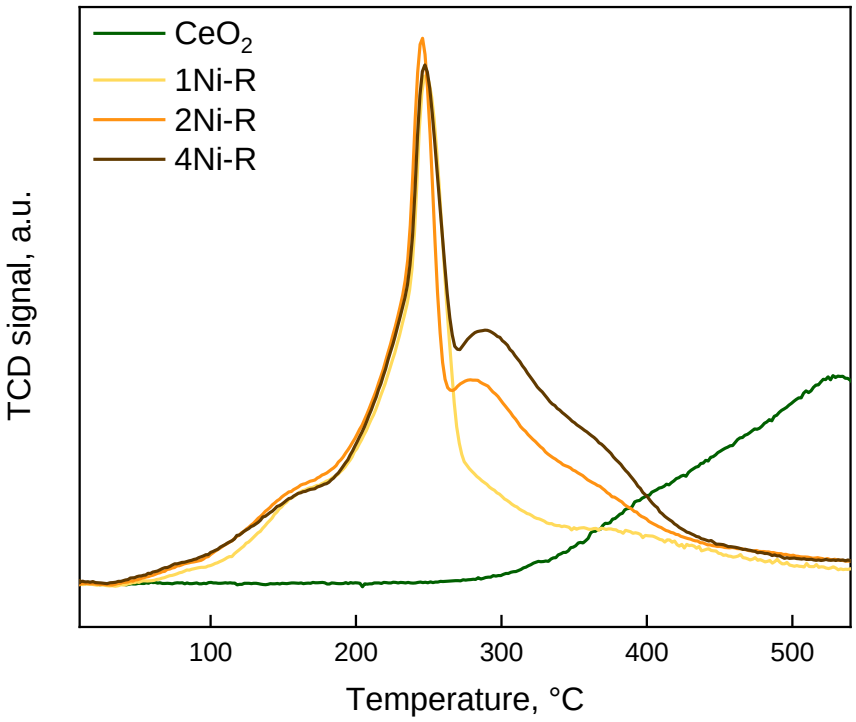

759

760 **Figure S 6.** H_2-TPR profiles of bare CeO_2-R and Ni/CeO_2 nanorod catalysts.

761

762

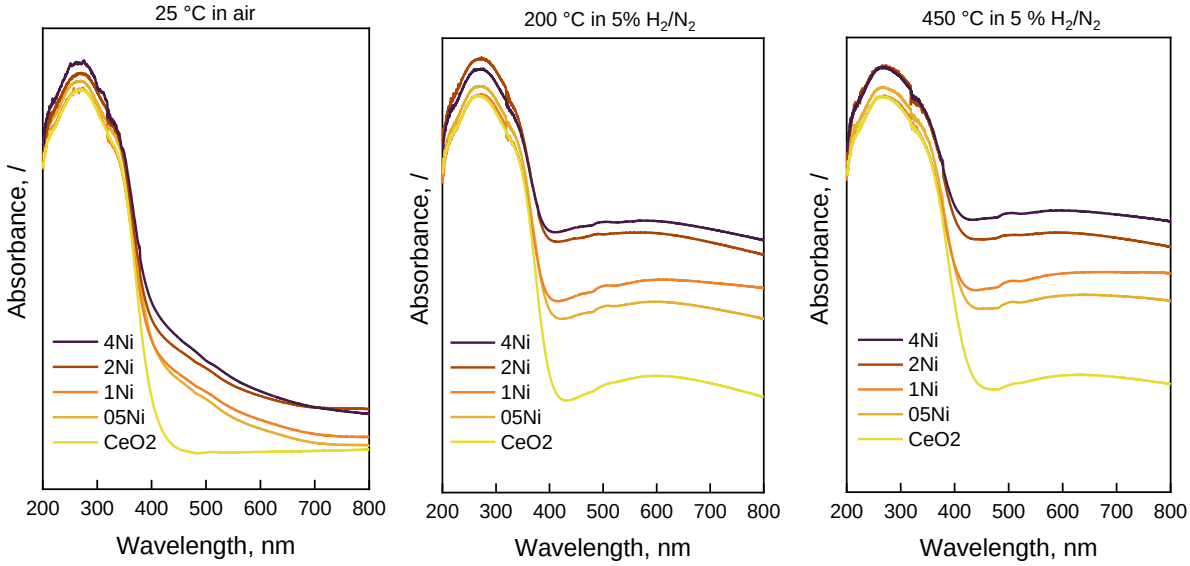

763 **Figure S 7.** *In-situ* UV-Vis DR spectra of bare CeO_2-R and Ni/CeO_2 nanorod catalysts in air at 25°C and

764 in 5% H_2/N_2 atmosphere at 200 and 450 °C.

765

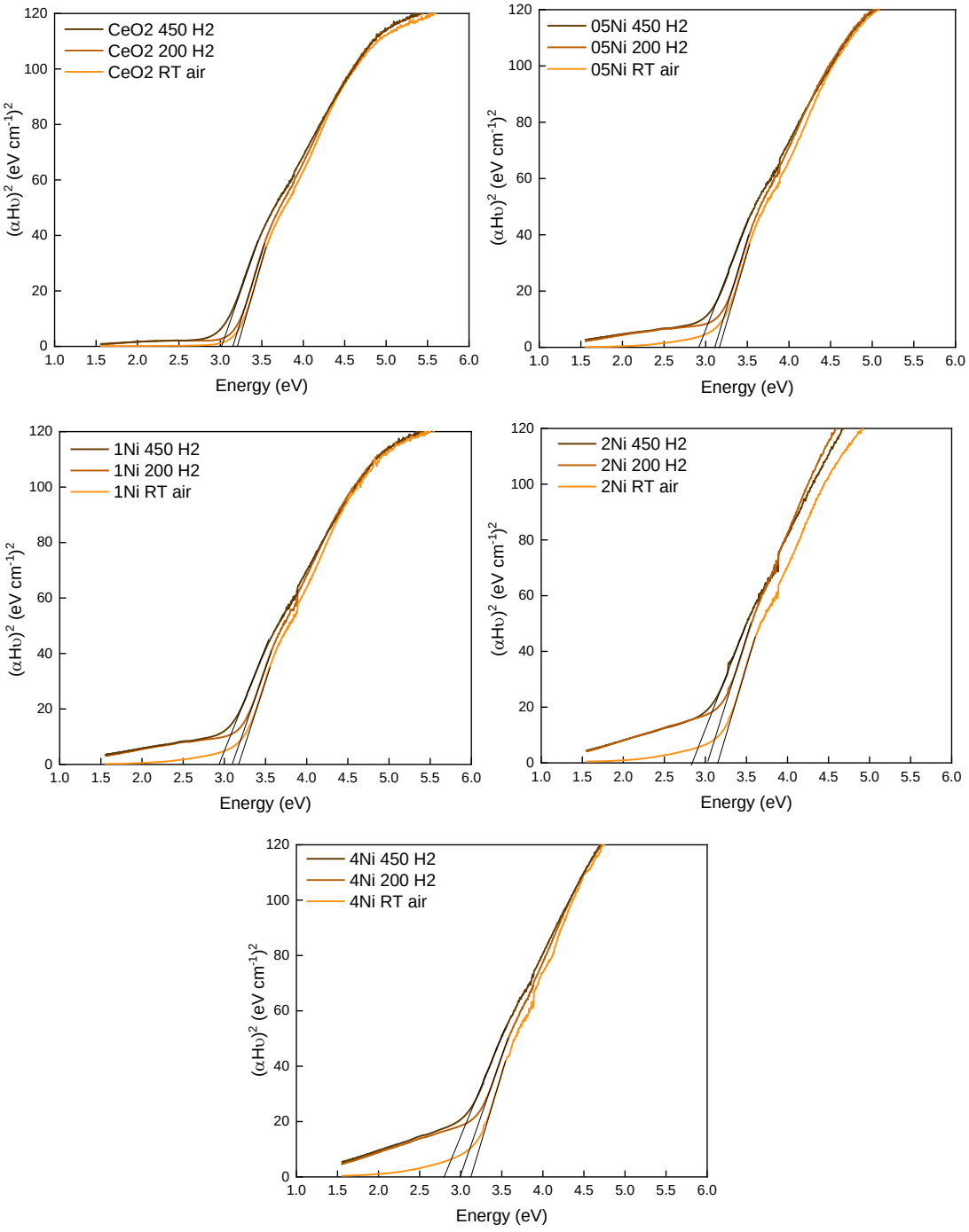

Figure S 8. Tauc plot analysis of optical bandgap energies for bare CeO_2-R and Ni/CeO_2 nanorod catalysts.

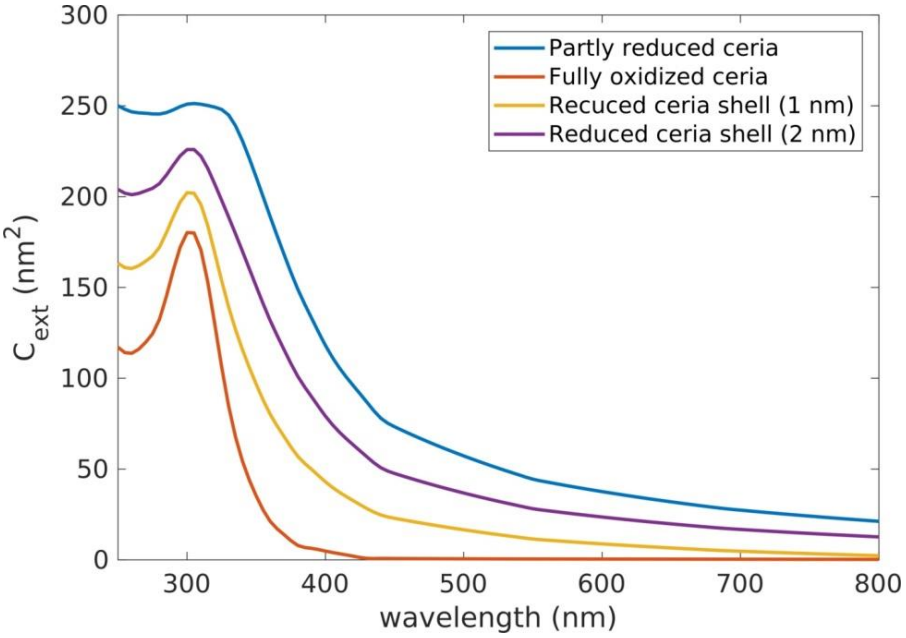

Figure S 9. Extinction cross-section for a *partly reduced* ceria nanorod (containing both Ce^{3+} and Ce^{4+})[1], *fully oxidized* CeO_2 (containing only the Ce^{4+})[2] and for a CeO_2nanorod, composed of a fully oxidized core and a reduced ceria shell with a thickness of 1 or 2 nm. The rods are assumed to be in an air-like environment. For the fully oxidized CeO_2, the optical constants for stoichiometric CeO_2 nano-crystalline transparent films[2] were used, while for partly reduced CeO_2, the optical constants of films heated in vacuum in an electron-beam-welded tungsten crucible for 2 hours at 2275 °C were taken from Marabelli and Wachter.[1]

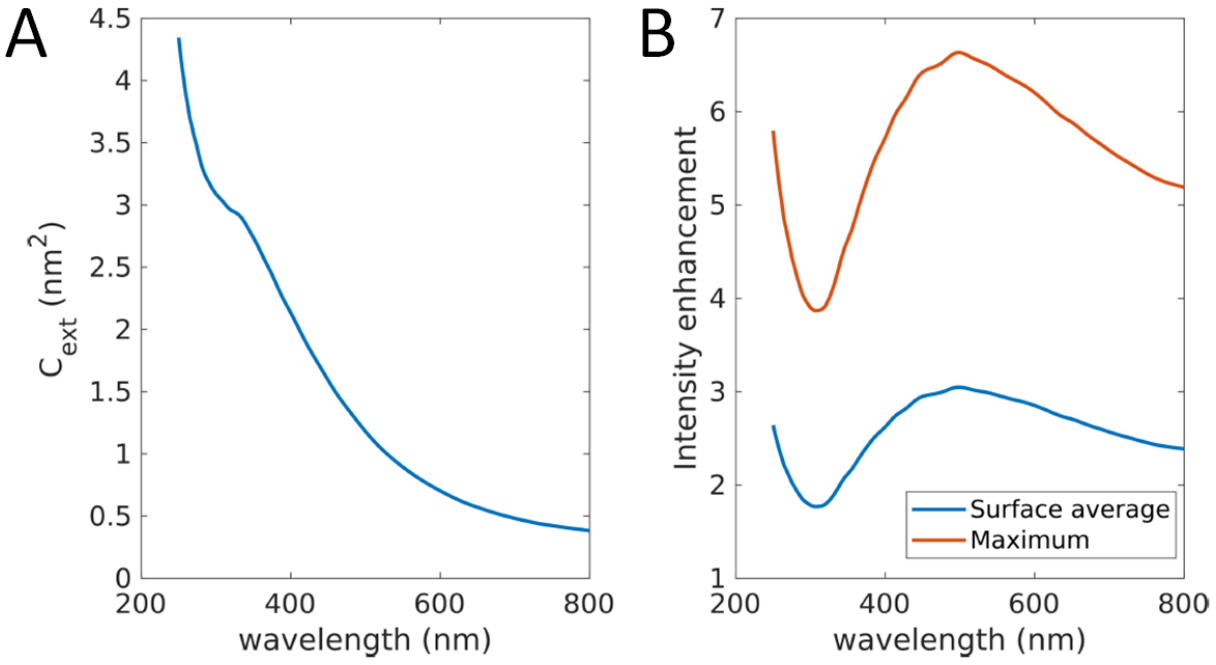

Figure S 10. (A) Extinction cross-section and maximum and (B) surface-averaged intensity enhancement over the particle surface for a Ni sphere 6 nm in diameter in an air-like environment. Optical constants for nickel were taken from reference[3].

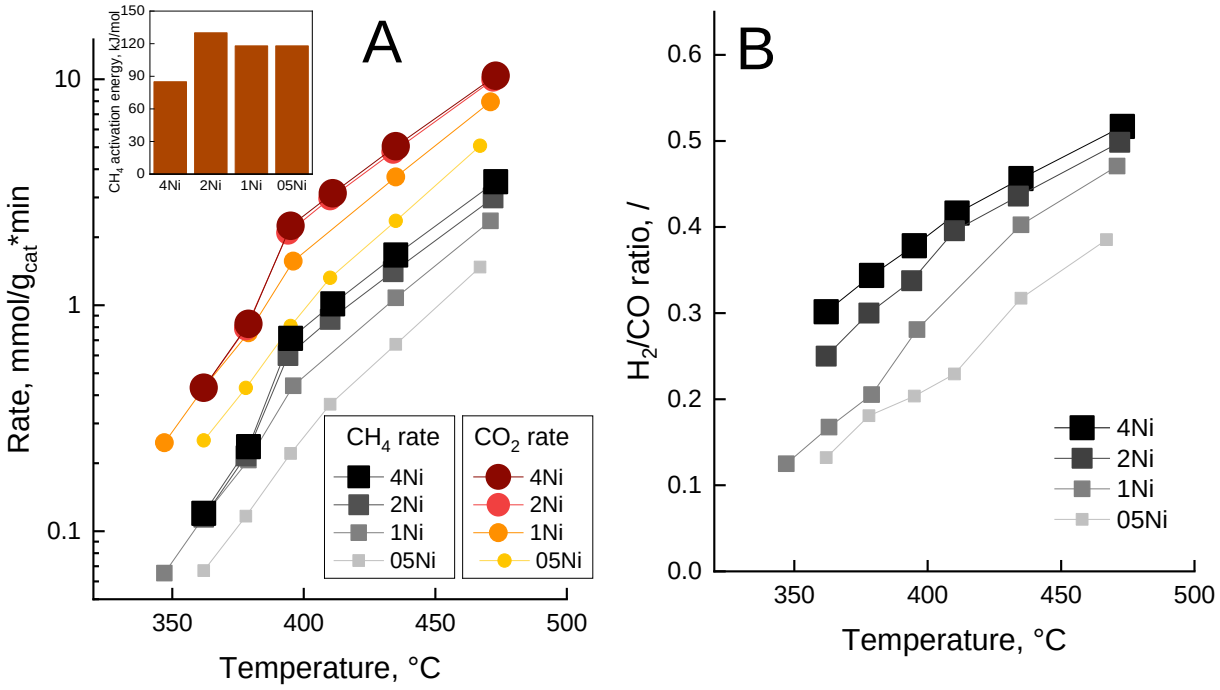

786 **Figure S 11.(**A) CH_4 and CO_2 reaction rates with calculated CH_4 activation energies (inset) and (B)
787 H_2/CO ratio as a function of catalyst temperature in the thermocatalytic regime over Ni/CeO_{2-x}
788 catalysts.
789

790

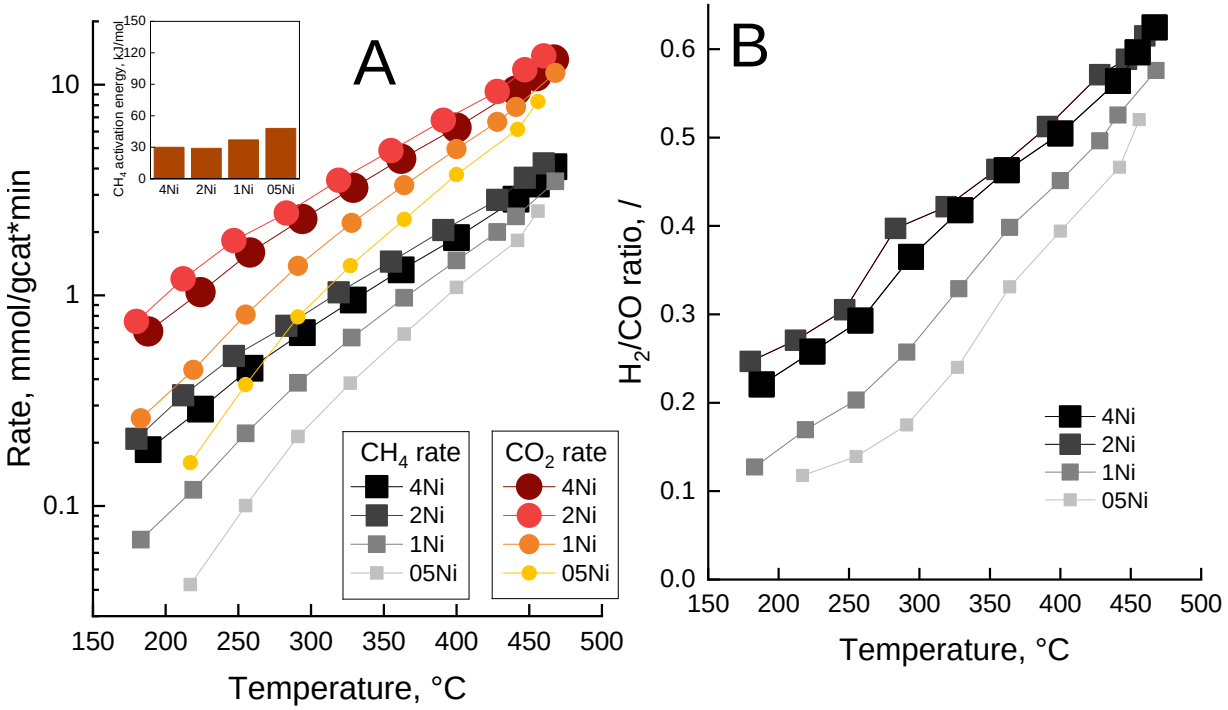

791 **Figure S 12.** A) CH_4 and CO_2 reaction rates with calculated CH_4 activation energies (inset); B) H_2/CO
792 ratio produced in the light assisted DRM over Ni/CeO_{2-x} catalysts.

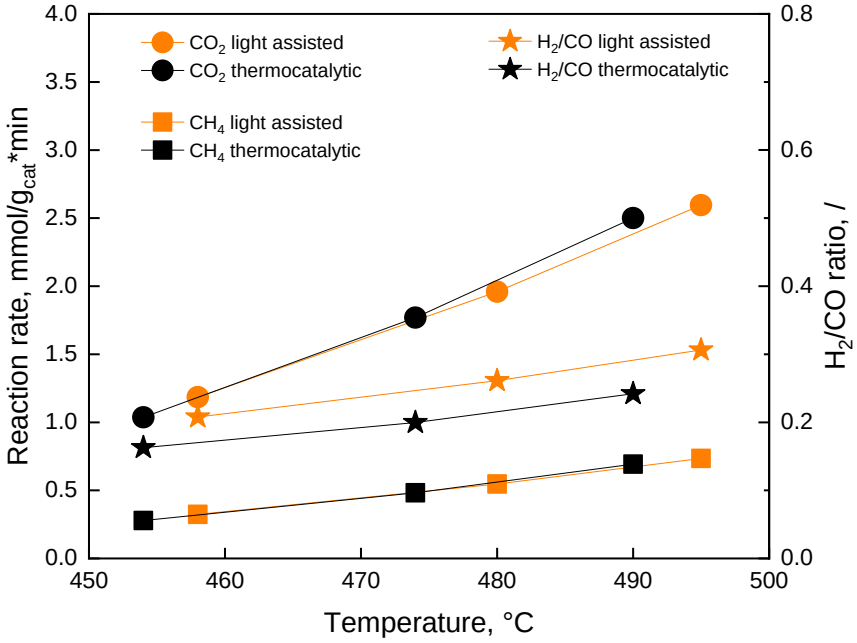

Figure S 13. Methane and CO_2 reaction rates during thermocatalytic (black symbols) and light assisted DRM reaction (orange symbols) over2Ni/SiO_2 catalyst. Reaction conditions: 2 mg of catalyst, $\Phi(CH_4)=\Phi(CO_2)$= 10ml/min, prior to catalytic tests, the sample was activated *in-situ* for 30 min at 450 °C in a 10 ml/min flow of 5% H_2/N_2. During the light assisted experiment, the catalyst was illuminated by 790 mW/cm^2 of white light.

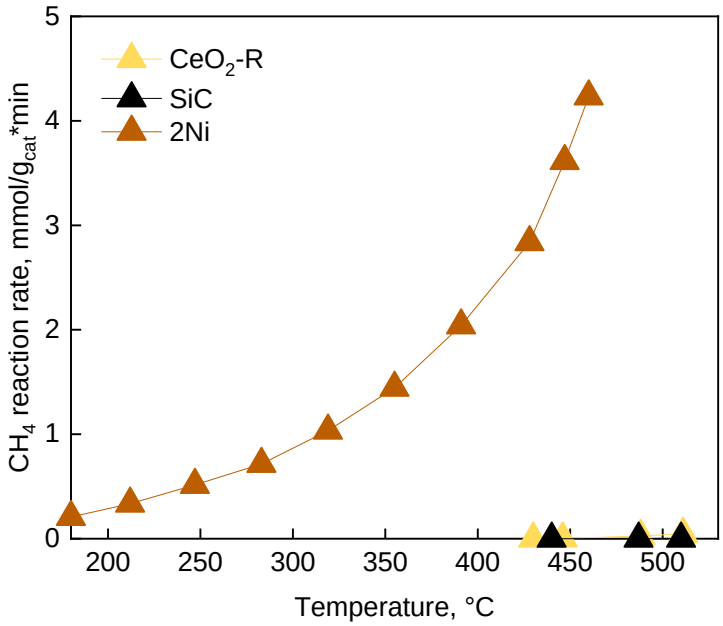

Figure S 14. CH_4 and CO_2 rates during light assisted DRM over 2Ni catalyst, bare CeO_2 nanorods (CeO_2-R) and SiC powder. SiC is completely inert, whereas ceria shows activity at 470 °C, which is about 1 % of that, measured over 2Ni catalyst at identical temperature.

P(*E*) is the probability of a hot carrier generation at energy *E* upon excitation by a photon of energy E_{ph}, DOS is density of states and f is a Fermi distribution function.[4–6]

Hot electron generation probability:

$$P(E) \propto DOS(E - E_{ph})f(E - E_{ph}) - DOS(E)[1 - f(E)]$$

Hot hole generation probability:

$$P(E) \propto DOS(E_{ph})f(E) - DOS(E + E_{ph})[1 - f(E+E_{ph})]$$

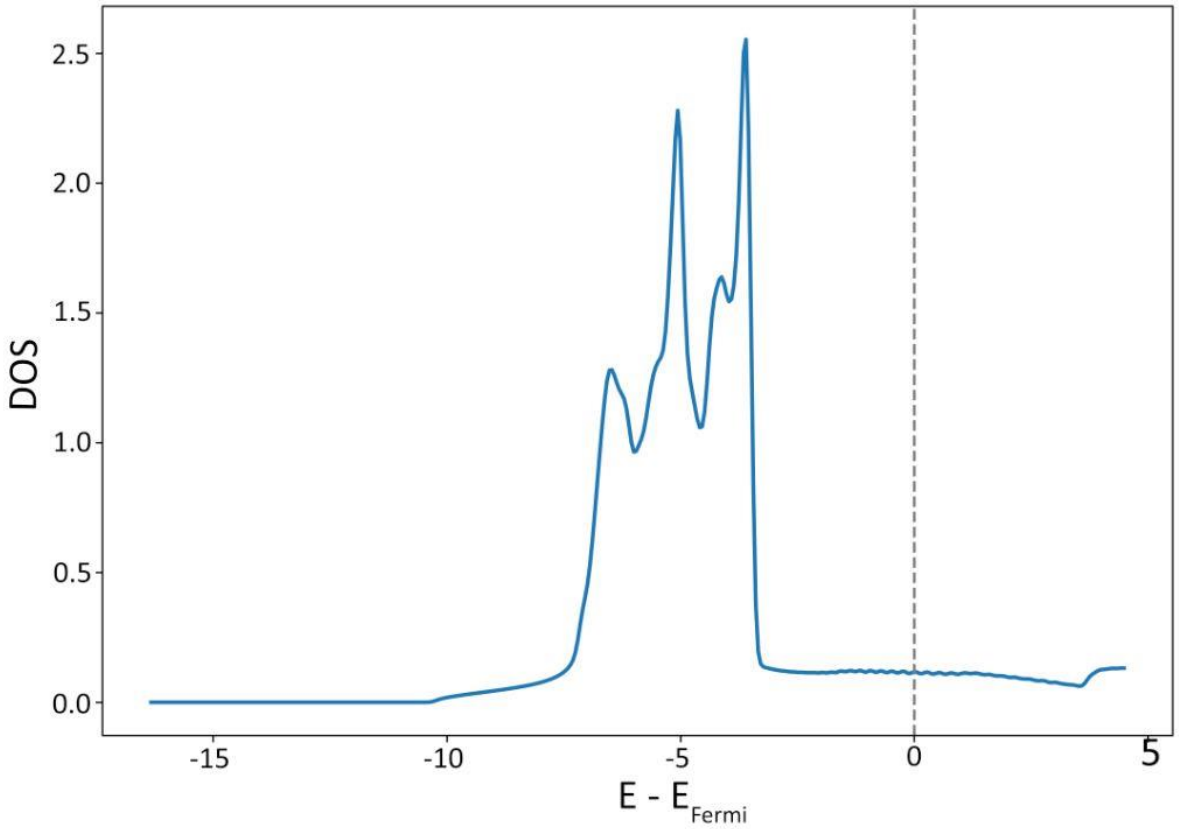

Figure S 15. The density of states for the ferromagnetic phase of bulk Ni with Fermi energy set to 0.

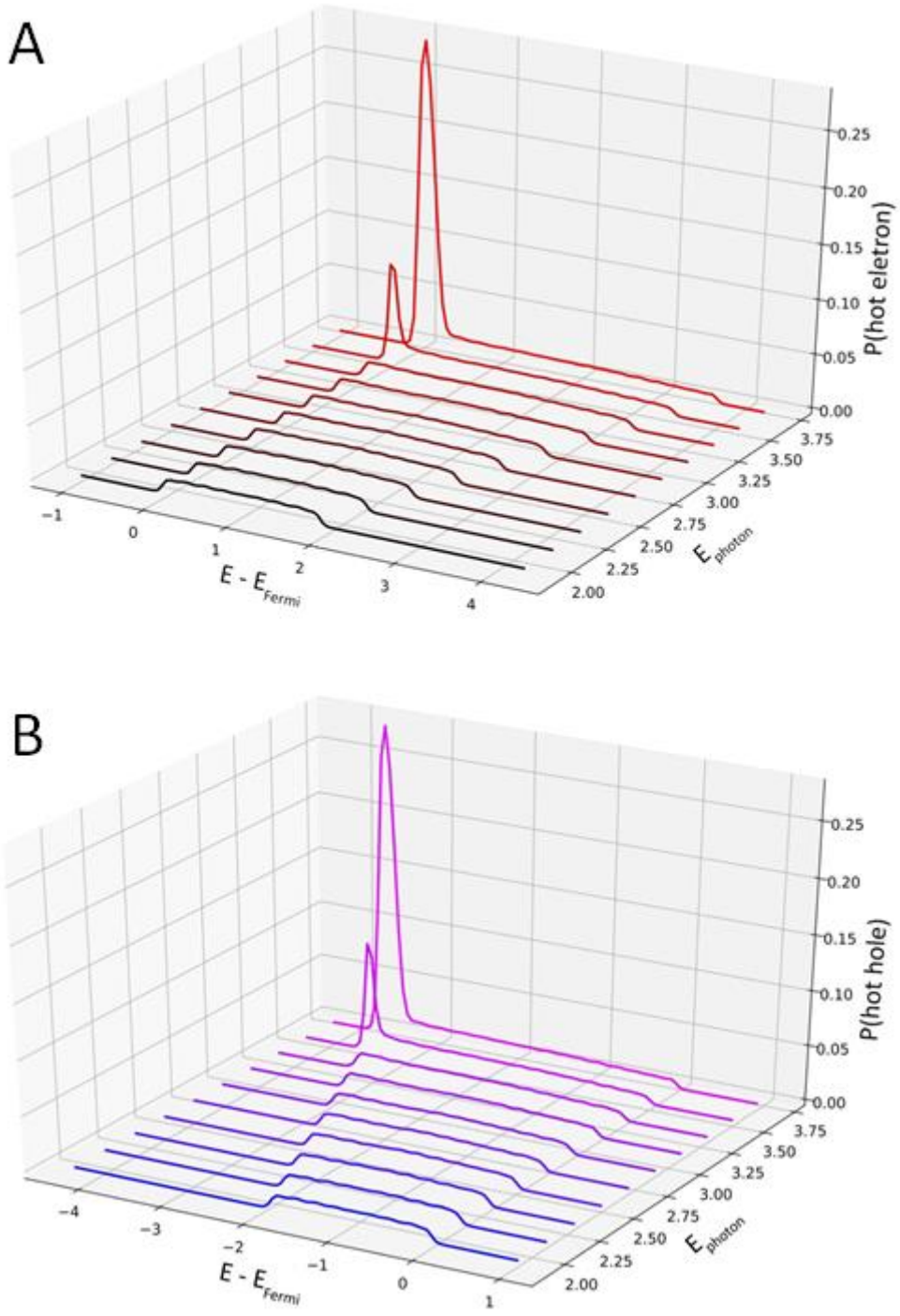

Figure S 16. (A) Relative probability distribution functions for hot electron and hot hole (B) generation in Ni for excitation by photon energies from 1.9 to 3.7 eV with an increment of 0.2. The distributions are flat in the visible range and show peaks only in UV for 3.5 and 3.7 eV. Relative probability is given in arbitrary units.

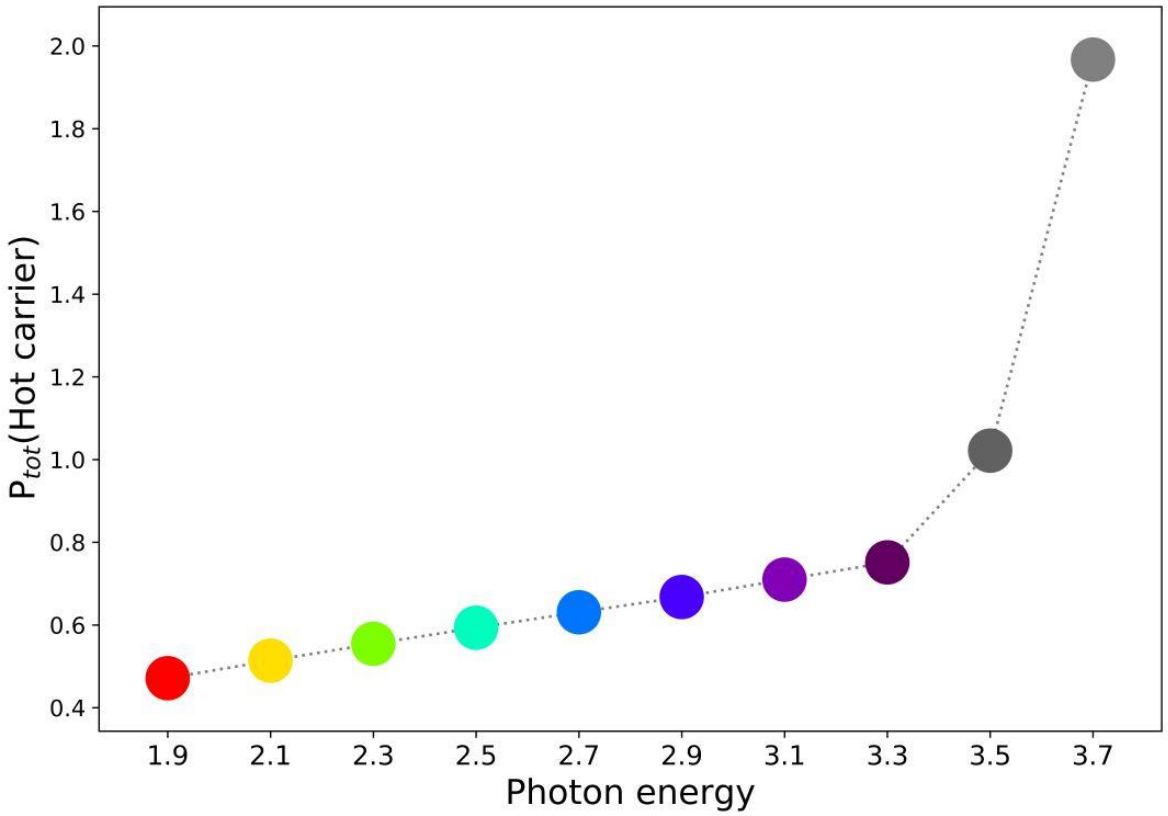

Figure S 17. Cumulative relative probability of hot carrier generation. Dots are colored by their respective photon energies in the visible range and shaded gray in the UV range. Relative probability is given in arbitrary units.

Supplementary references

(1) Marabelli, F.; Wachter, P. Covalent Insulator CeO2: Optical Reaectivity Measurements. *Phys. Rev. B* **1987**, *36* (2), 1238–1243.

(2) Patsalas, P.; Logothetidis, S.; Metaxa, C. Optical Performance of Nanocrystalline Transparent Ceria Films. *Appl. Phys. Lett.***2002**, *81* (3), 466–468.

(3) Palik, E. D. *Handbook of Optical Constants of Solids*; Academic press, 1998.

(4) Gong, T.; Munday, J. N. Materials for Hot Carrier Plasmonics. *Opt. Mater. Express***2015**, *5* (11), 2501.

(5) Krayer, L. J.; Palm, K. J.; Gong, C.; Torres, A.; Villegas, C. E. P.; Rocha, A. R.; Leite, M. S.; Munday, J. N. Enhanced Near-Infrared Photoresponse from Nanoscale Ag-Au Alloyed Films. *ACS Photonics***2020**, *7* (7), 1689–1698.

(6) Stofela, S. K. F.; Kizilkaya, O.; Diroll, B. T.; Leite, T. R.; Taheri, M. M.; Willis, D. E.; Baxter, J. B.; Shelton, W. A.; Sprunger, P. T.; McPeak, K. M. A Noble-Transition Alloy Excels at Hot-Carrier Generation in the Near Infrared. *Adv. Mater.***2020**, *32* (23), 1906478.